APPLIED SCIENCE & ENGINEERING TECHNOLOGY

WSRC-TR-95-0195
Task No.: Scoping

KEYWORDS:
Nuclear Fuel Storage
Canister Modeling
Natural Convection
Conduction Heat Transfer

Thermal Analysis Modeling And Simulation Of Spent Nuclear Fuel Canister Using CFDS-FLOW3D (U)

By

Si Y. Lee

ISSUED: April 1995

Savannah River Technology Center
Westinghouse Savannah River Company
Aiken, SC29808

Prepared for the U.S. Department of Energy
Under Contract DE-AC09-89SR18035

Document No.: WSRC-TR-95-0195
Title: Thermal Analysis Modeling And Simulation Of Spent Nuclear Fuel Canister Using CFDS-FLOW3D (U)
Task No.: Scoping
Task Title: Scoping

Approvals:

R. A. Dimenna, Technical Reviewer — Date: 5-11-95

J. R. Pelfrey, Manager, Engineering Modeling and Simulation Group — Date: 5-15-95

M. R. Buckner, Manager, Applied Technology Section — Date: 5/16/95

CONTENTS

LIST OF FIGURES

LIST OF FIGURES

LIST OF TABLES

Summary

The computational fluid dynamics (CFD) code CFDS-FLOW3D (version 3.3) has been utilized to model a three-dimensional thermal analysis of the spent nuclear fuel dry storage mockup test. The Experimental Thermal-Fluids (ETF) group obtained experimental data to benchmark computer codes for verifying the dry storage of aluminum-clad spent nuclear fuel.

This report provides CFDS-FLOW3D detailed predictions and benchmarks against the test data. Close comparison of the computational results with the experimental data provide verification that the code can be used to predict reasonably accurate convective flow and thermal behavior of a typical foreign research reactor fuel, such as the Material and Testing Reactor (MTR) design tested, while stored in a dry storage facility.

Introduction

The Experimental Thermal-Fluids (ETF) Laboratory has conducted a full-scale heat transfer experiment[1] for dry storage canister of aluminum-clad spent nuclear fuel to obtain an experimental database for the verification of computer codes. In the experiment, the instrumented fuel canister with imbedded electrical heater is surrounded by five unheated dummy canisters, and it is located inside a wind tunnel. Radial and axial heat flux/temperature profiles inside the fuel canister, air velocity outside the canister, and ambient temperature were measured. The canister diameter and height are 16" and 36", respectively. The canister will be filled with helium or nitrogen gas depending on the experiment. The sealed fuel can is located inside the canister and is designed to store four fuel assemblies. Each fuel assembly is separated by the stainless steel grid, and the natural convective flow induced by the buoyancy effect within each compartment of the four fuel assemblies can be communicated with each other only through the top and bottom slot holes inside the canister. The detailed descriptions for the internal geometry modeling of the fuel canister will be provided in next section.

The objective of this study is to perform thermal analysis calculations and benchmarks against the ETF test data for a given boundary condition using the computational fluid dynamics (CFD) code, CFDS-FLOW3D. These simulation results will provide verification that the CFD code can predict reasonably accurate thermal and gas flow behavior within a dry storage canister of a typical foreign research reactor fuel assembly, such as the Material and Testing Reactor (MTR). It is expected that CFDS-FLOW3D can be used to accurately predict temperatures of similar fuels in various storage configurations.

Description of CFDS-FLOW3D Solution Method and Model

CFDS-FLOW3D (version 3.3) CFD code has been used to model the 3-dimensional convective velocity and temperature distributions within a single dry storage canister of MTR fuel elements.

The analysis was mainly made for the temperature distributions and the buoyancy-driven flow field induced by the temperature gradient within an enclosed canister. Typical flow and temperature profiles under a natural convection mechanism are illustrated in Fig. 1. Temperature decreases rapidly due to the convective cooling effect within a boundary layer region, as shown in the illustration. The boundary layer flow is a buoyancy-induced motion resulting from body forces acting on density gradients which, in turn, arise from temperature gradients in the fluid. The gravitational body force is oriented in the negative z-direction for the present analysis. The governing equations for natural convection employed in CFDS-FLOW3D under the Cartesian coordinate system are shown below.

For the mass continuity,

$$\frac{\partial \rho}{\partial t} + \frac{\partial(\rho u)}{\partial x} + \frac{\partial(\rho v)}{\partial y} + \frac{\partial(\rho w)}{\partial z} = 0 \qquad (1)$$

For the momentum equation in tensor notation,

$$\rho\left(\frac{\partial u_i}{\partial t} + u_j \frac{\partial u_i}{\partial x_j}\right) = \frac{\partial \sigma_{ij}}{\partial x_j} + X_i$$

where the variables with the subscript, i (or j, k) = 1, 2, or 3, correspond to those of the x-, y-, or z-direction, respectively. σ_{ij} is the stress tensor and X_i the body force term.

$$\sigma_{ij} = -\left(P + \frac{2}{3}\mu \frac{\partial u_k}{\partial x_k}\right)\delta_{ij} + \mu\left(\frac{\partial u_i}{\partial x_j} + \frac{\partial u_j}{\partial x_i}\right)$$

$$\delta_{ij} = \begin{pmatrix} 1 & \text{for } i = j \\ 0 & \text{for } i \neq j \end{pmatrix}$$

$X_1 = X_2 = 0$ for the present model.

For the energy equation,

$$\rho\frac{Dh}{Dt} - \frac{\partial}{\partial x}\left\{k\frac{\partial T}{\partial x}\right\} - \frac{\partial}{\partial y}\left\{k\frac{\partial T}{\partial y}\right\} - \frac{\partial}{\partial z}\left\{k\frac{\partial T}{\partial z}\right\} - \frac{DP}{Dt} - \Phi - q''' = 0 \qquad (3)$$

where Φ is viscous dissipation term, h thermodynamic enthalpy, and q''' heat generation source term. The viscous dissipation term is not included in the present model.

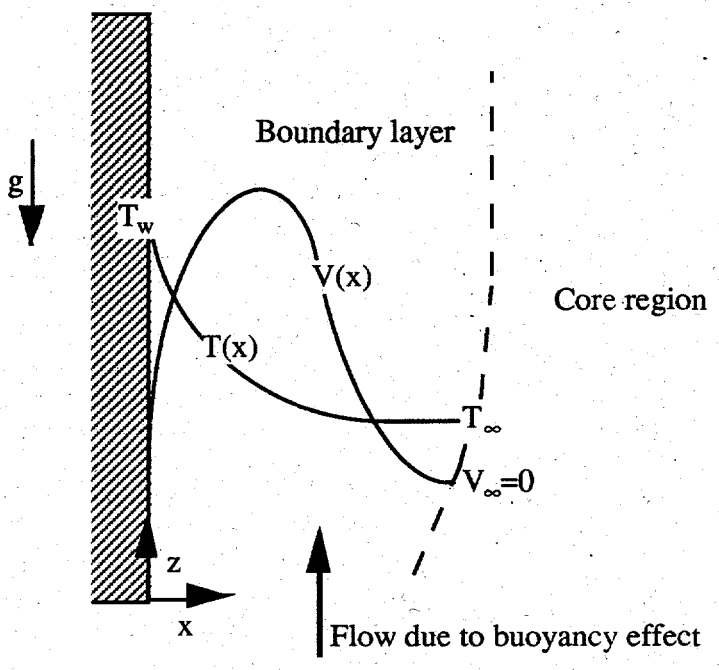

Figure 1. Typical temperature and velocity profiles in natural convective flow.

For the present analysis, the Boussinesq approximation was used for the consideration of buoyancy-driven natural convection. It is a two-part approximation: It neglects all variable property effects in the governing equations and it approximates the density difference term with a simplified equation of state, that is, the gravity term in the z-direction, $X_3 = -\rho g_z$, in eq. (2) is replaced by the following relation;

$$\rho g_z \rightarrow \rho\{1 - \beta(T - T_\infty)\}g_z \qquad (4)$$

where β is thermal expansion coefficient.

Natural convective flow regimes for each of the two cases in Table 1 may be estimated based on the non-dimensional quantity, Grashof number (Gr_z), which is the parameter describing the ratio of buoyancy to viscous forces:

For He-cooled canister (Case-I),

$$Gr_z = \frac{g\beta L^3(T_w - T_\infty)}{\nu^2} \qquad (5)$$

$$\approx 1.40 \times 10^7 < 1.0 \times 10^9 \text{ (laminar flow)}$$

where L = characteristic length parameter,
β = thermal expansion coefficient (= 2.85×10^{-3} K^{-1}),
T_∞ = ambient temperature,
ν = kinematic viscosity (= 1.593×10^{-4} m^2/sec).

Table 1. CFDS-FLOW3D model conditions for the present analysis.

Items		Case-I	Case-II
Coolant		He gas	N_2 gas
Canister internal structure		Identical	Identical
Boundary conditions	Canister outer wall surface	h = 6.81 W/mK	Variable (see Fig. 6) (8.5 to 13.2 W/mK)
	Top and bottom surfaces	Adiabatic	Adiabatic
Ambient temperature outside the canister		25 °C	23 °C
Internal heat source		100 W/bundle	100 W/bundle
Comparison of code predictions with experimental data		N/A	Done

For N_2-cooled canister (Case-II), Grashof number (Gr_z) is

$Gr_z \approx 3.60 \times 10^8$

where $\beta = 2.50 \times 10^{-3}\ K^{-1}$,
$\nu = 2.594 \times 10^{-5}\ m^2/sec.$

This corresponds to the near-transition flow. For the present analysis, natural convection regime within the canister is assumed to be laminar.

The 3-dimensional geometry file was created using the multi-block preprocessor of the CFDS-FLOW3D code under the body-fitted coordinate system, which allows the treatment of non-orthogonal geometry. Initially, an attempt was made to build the non-uniform fine meshing with progressive change of grid size near the conduction-convection interface to capture detailed temperature and velocity boundary layer behavior. The program could no longer be run on IBM RISC6000 because of the large memory requirements for larger than 10^5 grid cells. For the present analysis, optimum grids of 89632 were established from the grid sensitivity analysis under IBM RISC6000 environment.

The segregated solution technique was selected for the efficient run of the conduction-convection coupled problem with internal heat source. The linearized equations in each control volume were derived by integrating transport equations for mass, momentum, and energy at the center of each cell volume on the computational domain. The hybrid scheme of the Peclet number weighted central-forward differencing was used to obtain the finite difference approximations of continuity, momentum, and energy conservation equations for the fluid region. All variables such as u, v, w, P, and T are computed at the center of each node cell. CFDS-FLOW3D code used the non-staggered grid approach to obtain the velocity components on control volume faces from those on control volume centers by using the Rhie-Chow interpolation method since the staggered grid approach prohibitively requires large storage of geometric information to describe a fully non-orthogonal grid. The steady-state solution is desired, and this can be achieved either by advancing the governing equation set through a sequence of time steps or by dropping the transient term completely from the equations and using a purely iterative approach. For the present analysis, the first approach, that is, the quasi-steady approach was used by solving the transient equations. This approach was proven to be efficient method in the V&V test of the code[2].

In the CFDS-FLOW3D code, the complete set of governing equations is not solved simultaneously, namely, by a direct method since the direct method requires excessive computational effort. The CFDS-FLOW3D solution method ignores the non-linearity of the original differential equations. Thus, two levels of iteration are used: an inner iteration to solve for the spatial coupling for each variable and an outer iteration to solve for the coupling between variables. Each variable is taken in sequence with all other variables fixed so that a discretized transport equation for that variable is formed for every cell in the flow domain and the problem is handed over to a linear equation solver which returns the updated values of the variable. The non-linearity of the original equations is simulated by reforming the coefficients of the discrete equations, using the most recently computed values of the variables, before each inner iteration. However, the treatment of pressure is different from the foregoing description since it does not obey an original transport equation. Instead simplified versions of the discrete momentum equations are used to derive a functional relationship between a correction to the pressure and corrections to the velocity components in each cell. Substitution of this expression

into the continuity equation leads to an equation linking the pressure correction with the continuity error in each cell. The solution is used both to update pressure and to correct the velocity field through the pressure-velocity functional relationship in order to check the mass conservation. This numerical algorithm is known as the Semi-Implicit Method for Pressure-Linked Equations (SIMPLE) in the literature. The residual continuity error (ε_m) is obtained by substituting three pressure-corrected velocity components into the mass continuity equation for the cell control volume of Fig. 2. The resulting equation for ε_m becomes

$$\varepsilon_m = \left\{\frac{(\rho_P{}^o - \rho_P)\Delta x\Delta y\Delta z}{\Delta t}\right\} + \left\{(\rho u^*)_w - (\rho u^*)_e\right\}\Delta y\Delta z + \left\{(\rho v^*)_s - (\rho v^*)_n\right\}\Delta z\Delta x + \left\{(\rho w^*)_b - (\rho w^*)_t\right\}\Delta x\Delta y \qquad (6)$$

where superscript * denotes the velocity field based on a guessed pressure field p^*, and $\rho_P{}^o$ is the density at grid point P evaluated at old time step.

The residual term of the mass continuity, ε_m, in eq. (6) serves as an indicator of the convergence of the flow field solution in the CFDS-FLOW3D code. The iterations are continued until the ε_m values for every cell are within a tolerance, which is provided by the user input. It is noted that ε_m is a dimensional quantity (default unit: kg/sec). For the present analysis, the value of ε_m was used as 1.0×10^{-6} kg/sec for a convergence check.

The natural convection and conduction conjugate computational domain for the CFDS-FLOW3D 3-dimensional model is shown in Figure 3. Thermal radiation effect is assumed to be negligible compared to conduction and convection heat transfer mechanism since average temperature in the present analysis is generally low[3] and benchmarking results based on the conduction-convection model are in good agreement with the test data. Due to the computer resources limitation, only 90° sector of the test geometry was modeled using symmetrical condition of internal geometry for a single canister. Two symmetrical planes were taken through the center of the x- and y- planes (see Fig. 3). The dimensions of the canister, as modeled in CFDS-FLOW3D, are presented in Figs. 3 and 4. The narrow gas space (gap distance ≈ 0.33") between the inner and outer canister walls is assumed to be conduction-dominant. The interior of the canister in the model is filled with helium or nitrogen gas. The canister consists of 8 different layers and 32 mesh grids along the z-direction as illustrated in Fig. 4. Non-uniform mesh grids on the x-y plane of the present model are illustrated in Fig. 5. Figure 6 presents 3-dimensional grid meshes (89632 meshes) as is modeled in the code. The two different cases are studied here as shown in Table 1. They are He-gas filled spent fuel canister with constant wall heat transfer coefficient and N_2 gas-filled canister with variable wall heat transfer coefficient boundary condition. Figure 7 shows variable heat transfer coefficient as a function of azimuthal position around the canister wall to provide the wall boundary condition to the FLOW3D model for Case-II. CFDS-FLOW3D actually used the discretized wall boundary for computational efficiency. Top and bottom surfaces of the canister are assumed to be adiabatic. The thermal properties used in the code predictions for each case are presented in Tables 2 and 3.

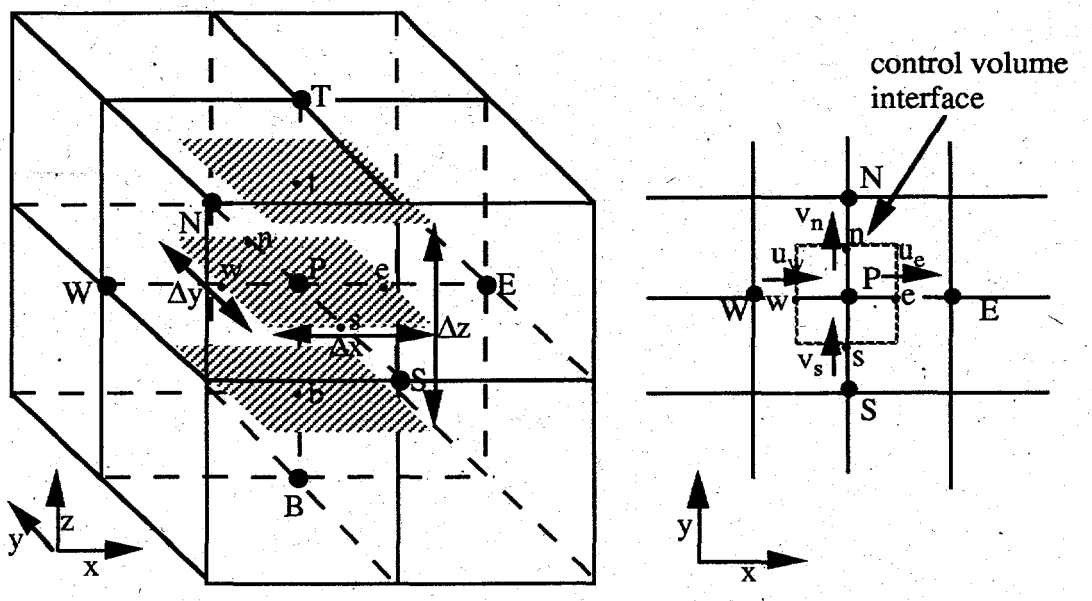

3-dimensional control volume

2-dimensional control volume

Figure 2. Control volume and its neighboring points for a single cell.

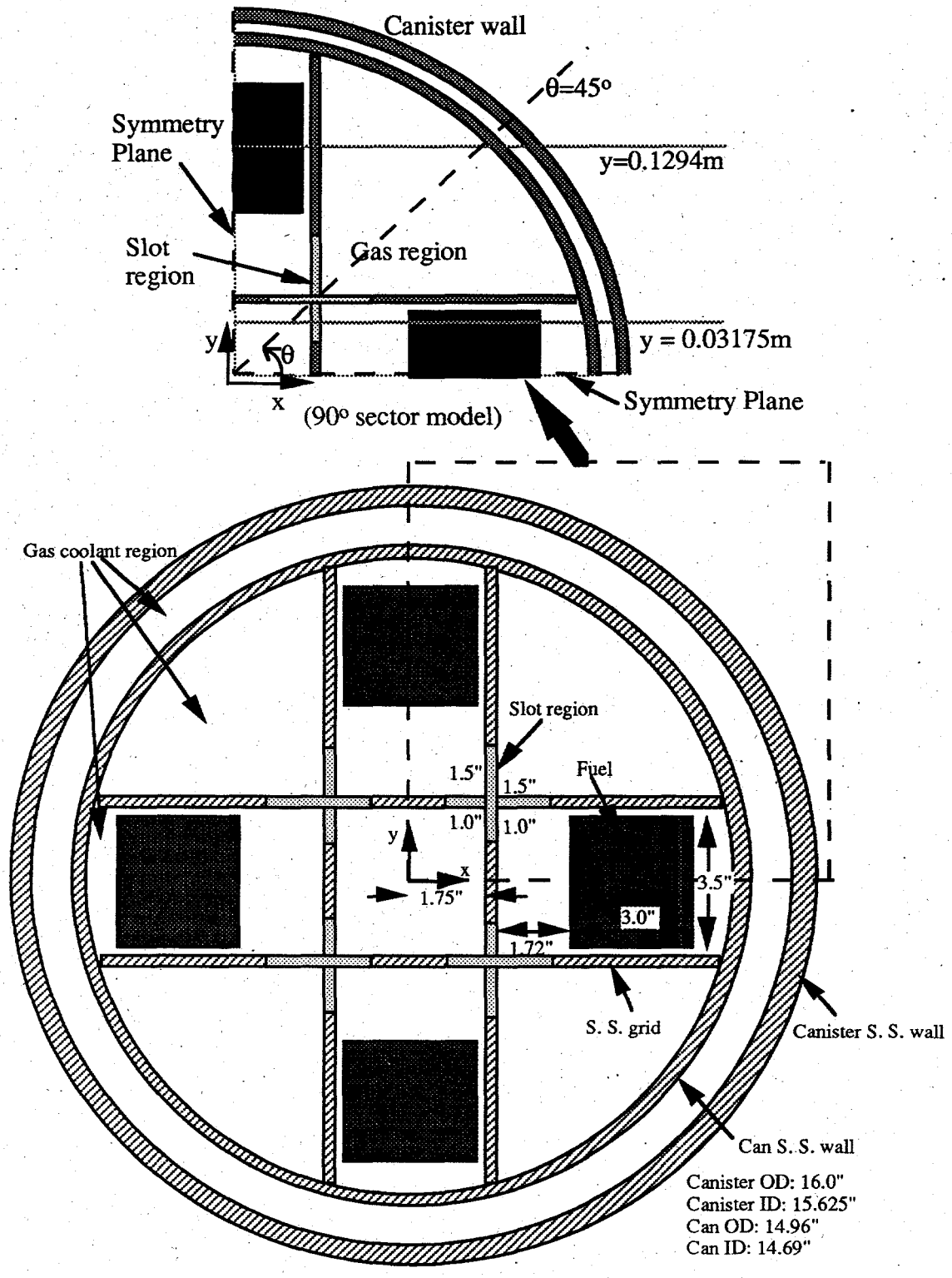

(original prototypic geometry)

Figure 3. Cross-sectional view of the CFDS-FLOW3D 90° sector model (slot is open only near top and bottom regions).

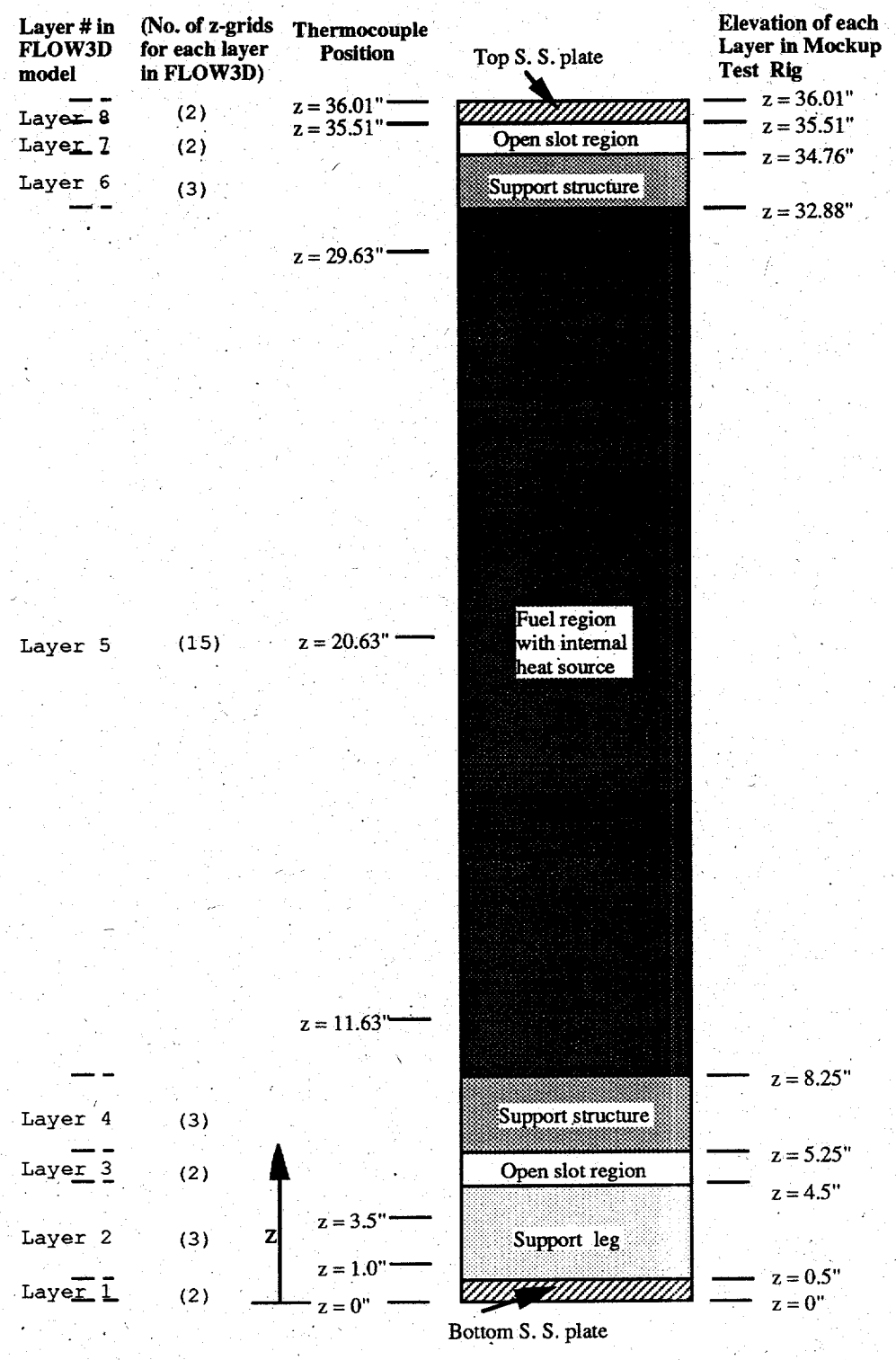

Figure 4. Experimental thermocouple positions and elevation heights of 8 layers in the CFDS-FLOW3D model.

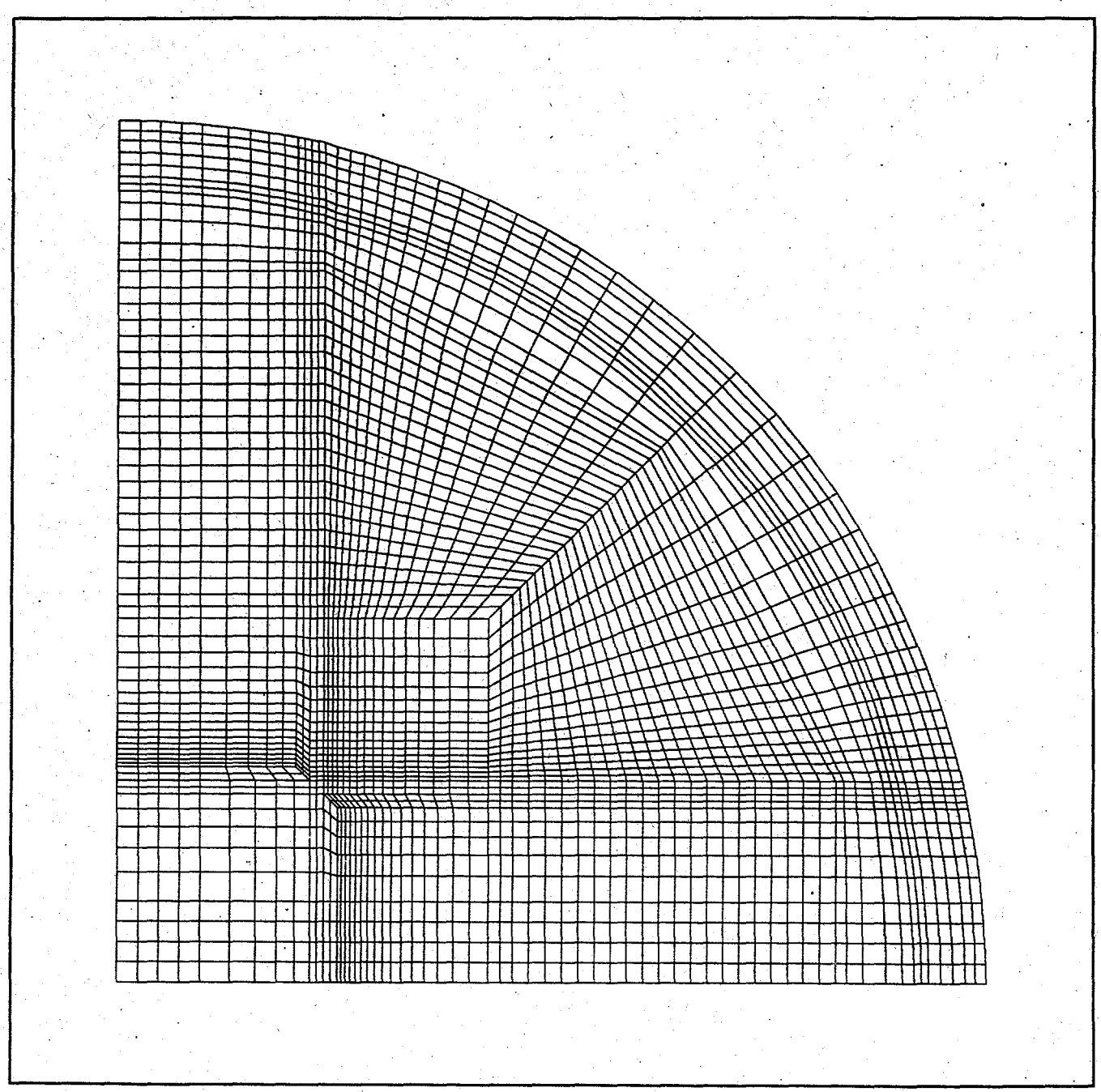

Figure 5. Mesh grids in the x-y plane of the CFDS-FLOW3D model.

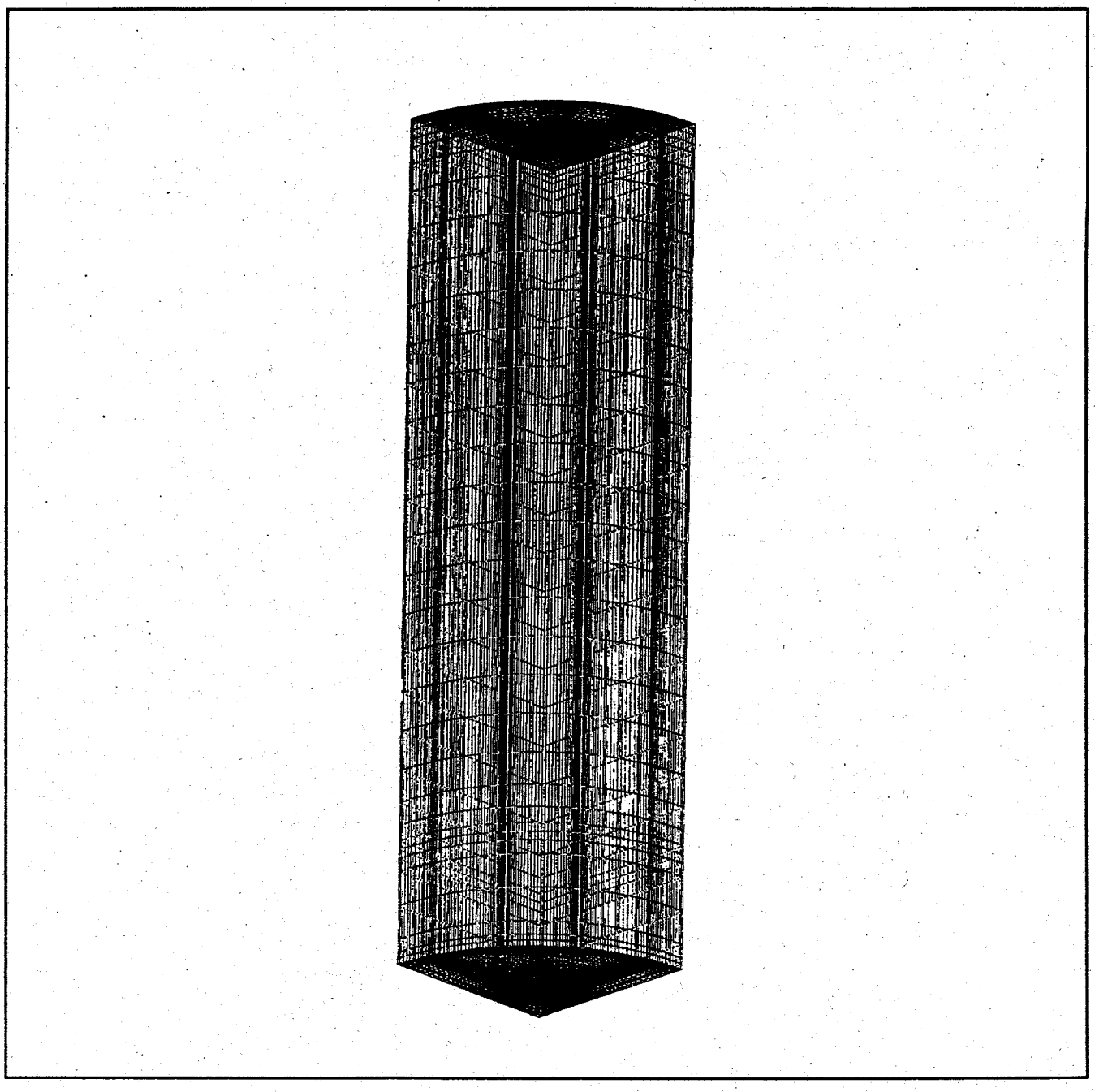

Figure 6. 3-dimensional mesh grids in the CFDS-FLOW3D model.

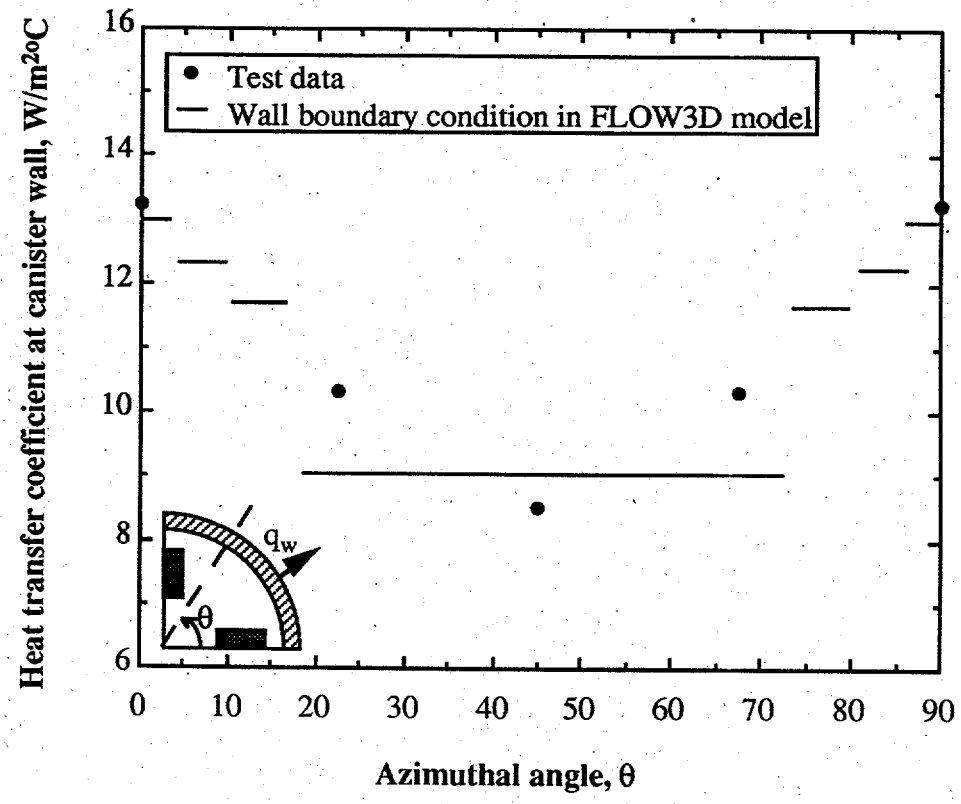

Figure 7. Heat transfer coefficients around the SNF (Spent Nuclear Fuel) canister wall (Case-II).

Table 2. Thermal properties for heat conduction regions within a canister in 3-dimensional heat transfer model (Case-I).

Layer # within a canister	Structural Material Region	Thermal Conductivity (W/mK)
Layer 1	Bottom s. s. plate	17.30
Layer 2	Inner and outer wall regions (s. s.)	17.30
	Gas region (He gas)	0.173
	Grid region near wall	0.865
	Main grid region	17.30
	Extended fuel region	17.30
Layer 3	Inner and outer wall regions (s. s.)	17.30
	Gas region (He gas)	0.173
	Grid region near wall	0.865
	Main grid region	17.30
	Extended fuel region	24.739
Layer 4	Inner and outer wall regions (s. s.)	17.30
	Gas region (He gas)	0.173
	Grid region near wall	0.865
	Main grid region	17.30
	Extended fuel region	20.760
Layer 5	Inner and outer wall regions (s. s.)	17.30
	Gas region (He gas)	0.173
	Grid region near wall	0.865
	Main grid region	17.30
	Main fuel region with heat source	34.600
Layer 6	Inner and outer wall regions (s. s.)	17.30
	Gas region (He gas)	0.173
	Grid region near wall	0.865
	Main grid region	17.30
	Extended fuel region	24.739
Layer 7	Inner and outer wall regions (s. s.)	17.30
	Gas region (He gas)	0.173
	Grid region near wall	0.865
	Main grid region	17.30
	Extended fuel region	0.519
Layer 8	Top s. s. plate	17.30

Note: Layer # within a canister is shown in Fig. 4.

Table 3. Thermal properties for heat conduction regions within a canister in 3-dimensional heat transfer model (Case-II).

Layer # within a canister	Structural Material Region	Thermal Conductivity (W/mK)
Layer 1	Bottom s. s. plate	17.30
Layer 2	Inner and outer wall regions (s. s.)	17.30
	Gas region (N_2 gas)	0.03
	Grid region near wall	0.865
	Main grid region	17.30
	Extended fuel region	17.30
Layer 3	Inner and outer wall regions (s. s.)	17.30
	Gas region (N_2 gas)	0.03
	Grid region near wall	0.865
	Main grid region	17.30
	Extended fuel region	24.739
Layer 4	Inner and outer wall regions (s. s.)	17.30
	Gas region (N_2 gas)	0.03
	Grid region near wall	0.865
	Main grid region	17.30
	Extended fuel region	20.760
Layer 5	Inner and outer wall regions (s. s.)	17.30
	Gas region (N_2 gas)	0.03
	Grid region near wall	0.865
	Main grid region	17.30
	Main fuel region with heat source	34.600
Layer 6	Inner and outer wall regions (s. s.)	17.30
	Gas region (N_2 gas)	0.03
	Grid region near wall	0.865
	Main grid region	17.30
	Extended fuel region	24.739
Layer 7	Inner and outer wall regions (s. s.)	17.30
	Gas region (N_2 gas)	0.03
	Grid region near wall	0.865
	Main grid region	17.30
	Extended fuel region	0.519
Layer 8	Top s. s. plate	17.30

Note: Layer # within a canister is shown in Fig. 4.

Results and Discussions

The 3-dimensional analysis was made for two cases, Case-I and Case-II, with q'''=100 watts per MTR fuel element (equivalent to 25.410 kW/m^3) and h = 1.8 Btu/hr ft^2°F (≈ 10.3 W/m^{2}K) using the same FLOW3D geometry file. The maximum fuel temperature was computed for the conduction only, assuming that gas flow motion within the canister is frozen completely, and for the conduction-convection coupled problem. The results are presented in Table 4. Maximum temperature for Case-II is higher than that of Case-I since He thermal conductivity is about 6 times higher than that of N_2 gas in Case-II.

Table 4. Maximum temperature and canister outer wall temperature predicted by the CFDS-FLOW3D model for each case.

Cases	Conduction Only	Conduction-Convection	
	Max. Temperature	Max. Temperature	Canister wall surface temperature at fuel mid-plane and θ = 45°
Case-I	143 °C	136 °C	about 72°C
Case-II	210 °C	194 °C	about 47 °C

The temperature profile predicted by the conduction model is compared with that of the conduction-convection conjugate model for Case-I as shown in Fig. 8. The cooling effect due to the buoyancy-driven flow motion is about 20 °C max. difference at the center of fuel canister for this case. For Case-II, the conduction results are higher than those of the conduction-convection case by 45 °C maximum difference at the center of the canister. The comparisonal results are shown in Fig. 9.

Figure 10 shows the computational results for Case-I and -II along the constant line, y=0.03175 m, at the fuel mid-height plane. It is noted that temperature gradient within a thermal boundary layer near the conduction-convection interface for Case-II is much larger than that of Case-I. The buoyancy-induced flow velocity profiles corresponding to these temperature gradients are also shown in Fig. 11.

The gas near the central region within an enclosed canister is moving upward like a gas plume, while the gas near the cooler space like the near-wall region is moving downward due to the gravity effect. The gas flow pattern over the entire flow domain within the canister is illustrated in Fig. 12 from the computational results for Case-I and -II. The results clearly show that there are two main flow circulation loops within the canister. The hot gas near the central region goes up due to buoyancy and passes through the open top slot region (0.75" in slot height) into the near-wall corner of the vacant quadrant, and it then goes downward along the near-wall corner region. The gas cooled by the convective wall boundary condition reaches the bottom slot region, and it is divided into two gas upstreams. One gas stream goes up through the corner near the empty quadrant

adjacent to the mockup fuel element, and the other goes up along the central region of the canister through the open bottom slot.

Figures 13 through 17 present flow velocity vector plots near top/bottom slot regions and for two vertical planes (y = 0.03175 m and y= 0.1294 m in the 90° sector model of Fig. 3) in Case-I. The gas region near the center of the canister is hotter compared with that of the near-wall boundary region as shown in Fig. 18. Temperature contour plots for the two vertical planes are shown in Figs. 19 and 20. The results show that maximum fuel temperature occurs near the top of the mockup fuel element.

For N_2 gas-cooled design with variable convective boundary conditions (Case-II), velocity vector plots along the vertical plane at y=0.03175 m and on the horizontal planes (top/bottom slot regions and middle height of fuel region) are presented in Figs 21 through 26. It is noted that there are two vortices near the top/bottom open slot region as shown in Figs. 21 and 23. This indicates the near-transition regime to the turbulent flow in the natural convection flow ($Gr_z \approx 10^9$) as described in the previous section. Temperature contour plots on the fuel mid-plane and the vertical plane of y = 0.03175 m are also shown in Figs. 27 and 28. Figure 27 shows that temperature for the stainless steel grid region, which locates very close to the fuel wall surface (gap size between grid and fuel wall = 0.125"), is hotter than the surrounding gas temperature since natural convective cooling effect is small compared to conduction effect within the narrow air gap and nitrogen gas thermal conductivity is very small compared to that of stainless steel grid.

Finally, the code predictions (Case-II) for the MTR mockup fuel region along the vertical direction are benchmarked against the ETF test data. The results are shown in Fig. 29. In addition, the computational results for the temperature distribution along the y= 0.1294 m line on the mid-plane of the fuel region are compared with the experimental data as shown in Fig. 30. Figure 31 shows the velocity profile corresponding to the temperature distribution presented in Fig. 30. It is shown that large temperature and velocity gradients within natural convection boundary are established near the solid boundary. The benchmarking results for Case-II are shown to be in good agreement with the ETF test data within less than 10 %.

Conclusions

CFDS-FLOW3D (version 3.3) predictions of temperature and flow velocity distributions with the 3-dimensional conduction-convection conjugate models were completed for He-cooled canister with constant convective boundary (Case-I) and N2-cooled canister with variable convective boundary (Case-II). The conduction calculations for both cases were also performed to evaluate the effect of natural convective cooling in the dry storage design. The computational results are consistent with natural convection phenomena in the literature and are validated by the simulation results (Ref. 2). The benchmarking results are also shown to be in good agreement with the ETF test data.

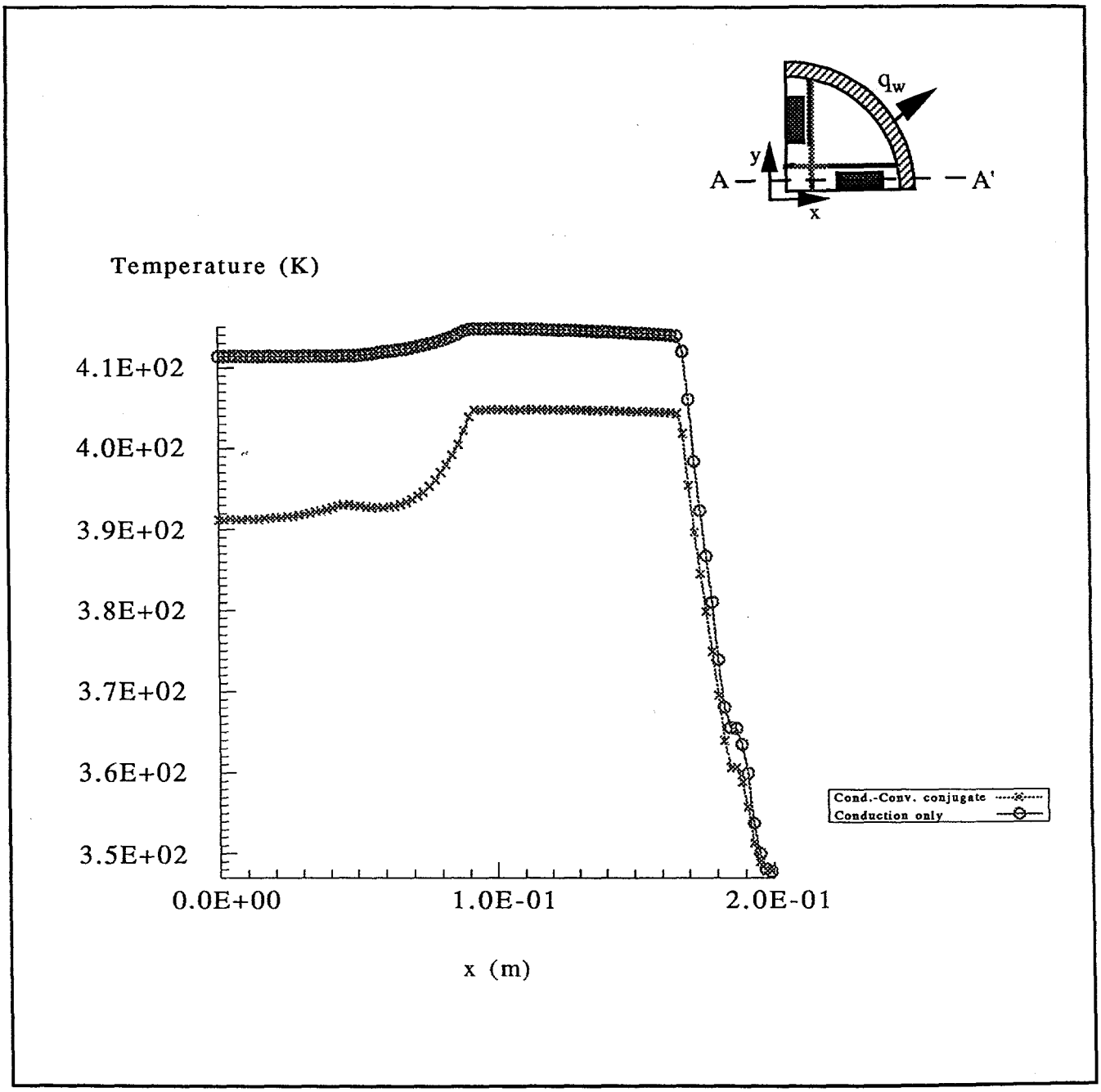

Figure 8. Comparison of temperature profiles for the conduction model with those of conduction-convection conjugate model along the A-A' line (y=0.03175m) of the fuel mid-plane in Case-I.

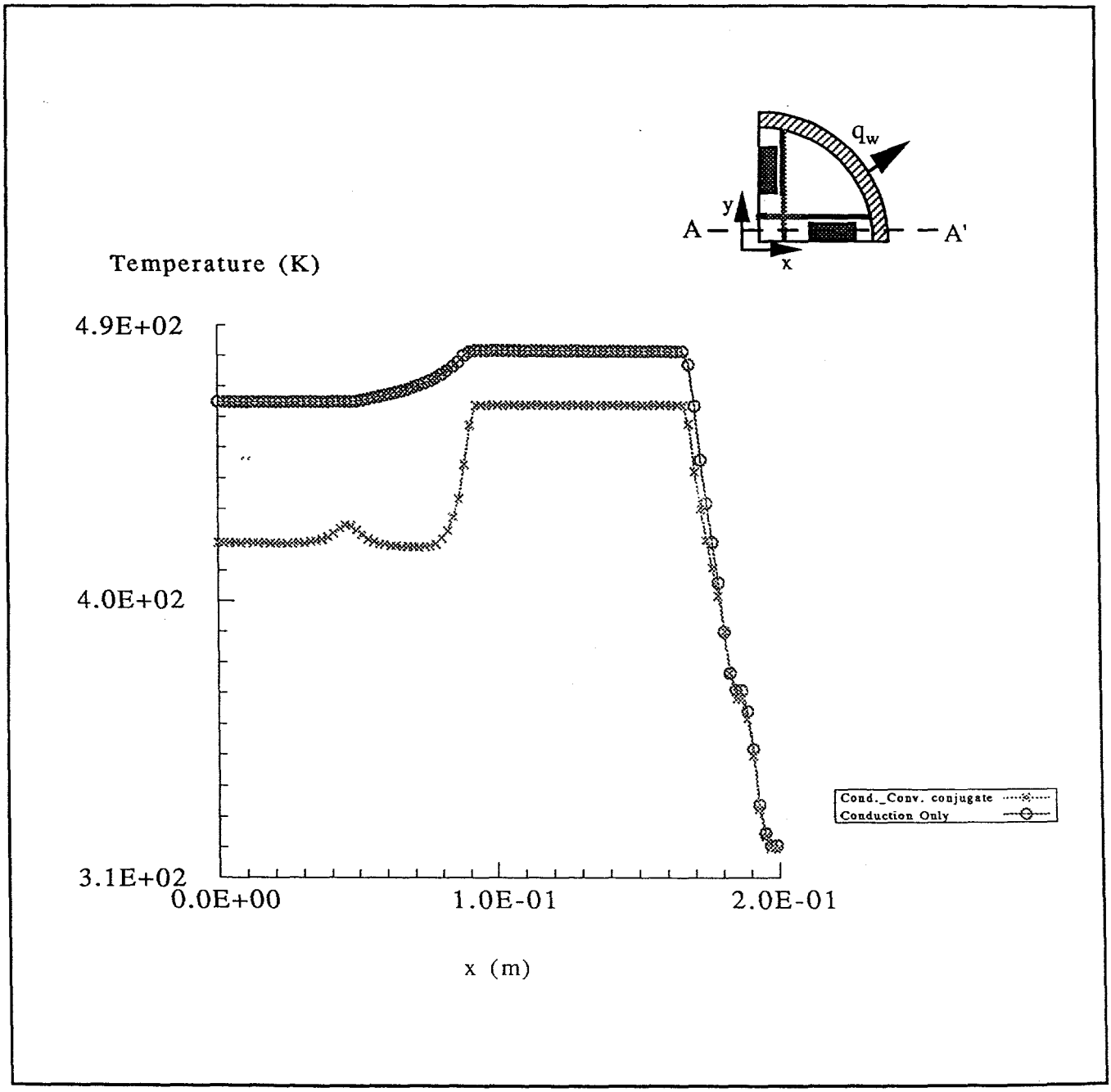

Figure 9. Comparison of temperature profiles for the conduction model with those of conduction-convection conjugate model along the A-A' line (y=0.03175m) of the fuel mid-plane in Case-II.

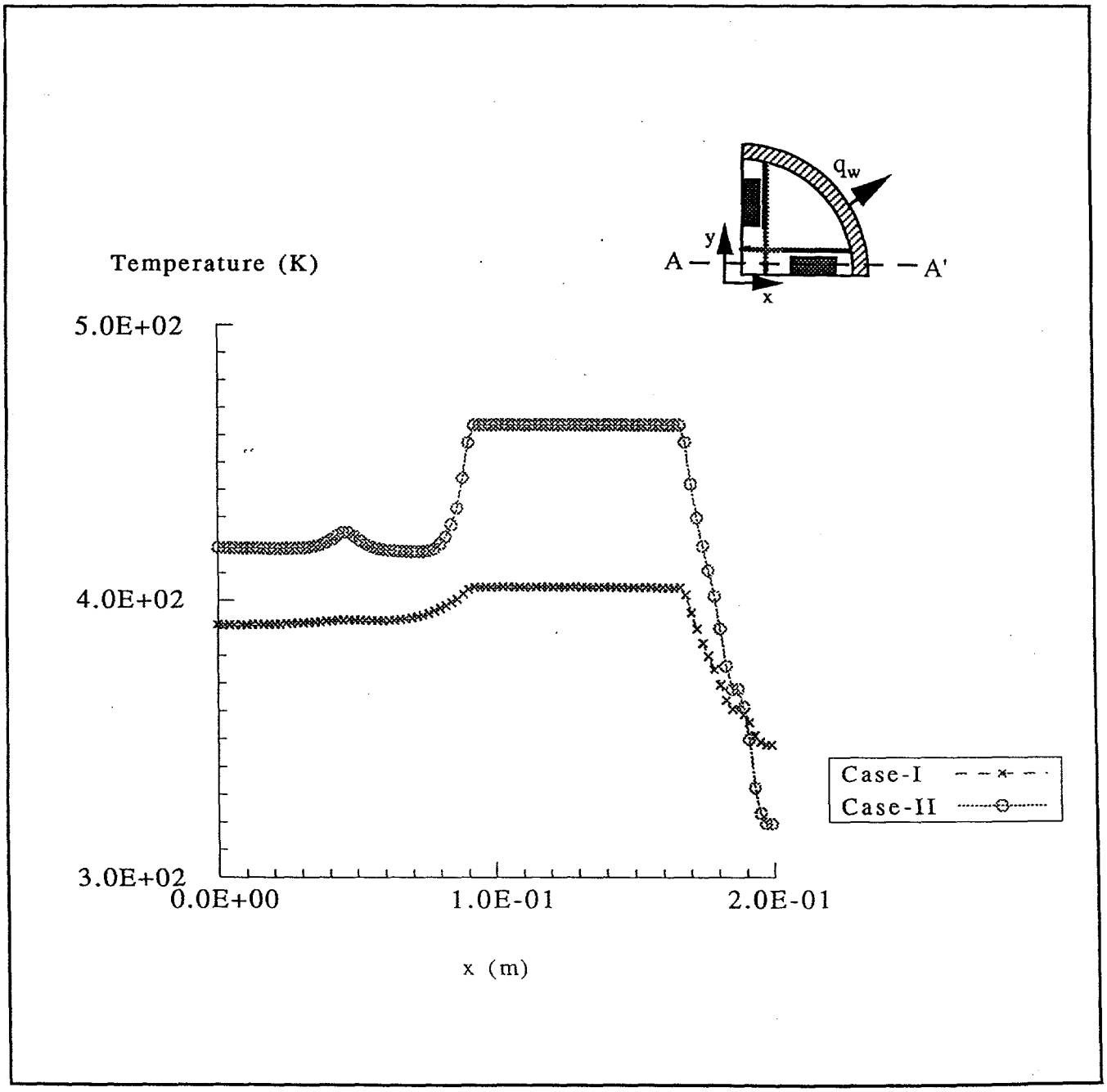

Figure 10. Temperature profiles for the conduction-convection model in Case-I and -II along the A-A' line (y=0.03175m) of the fuel mid-plane.

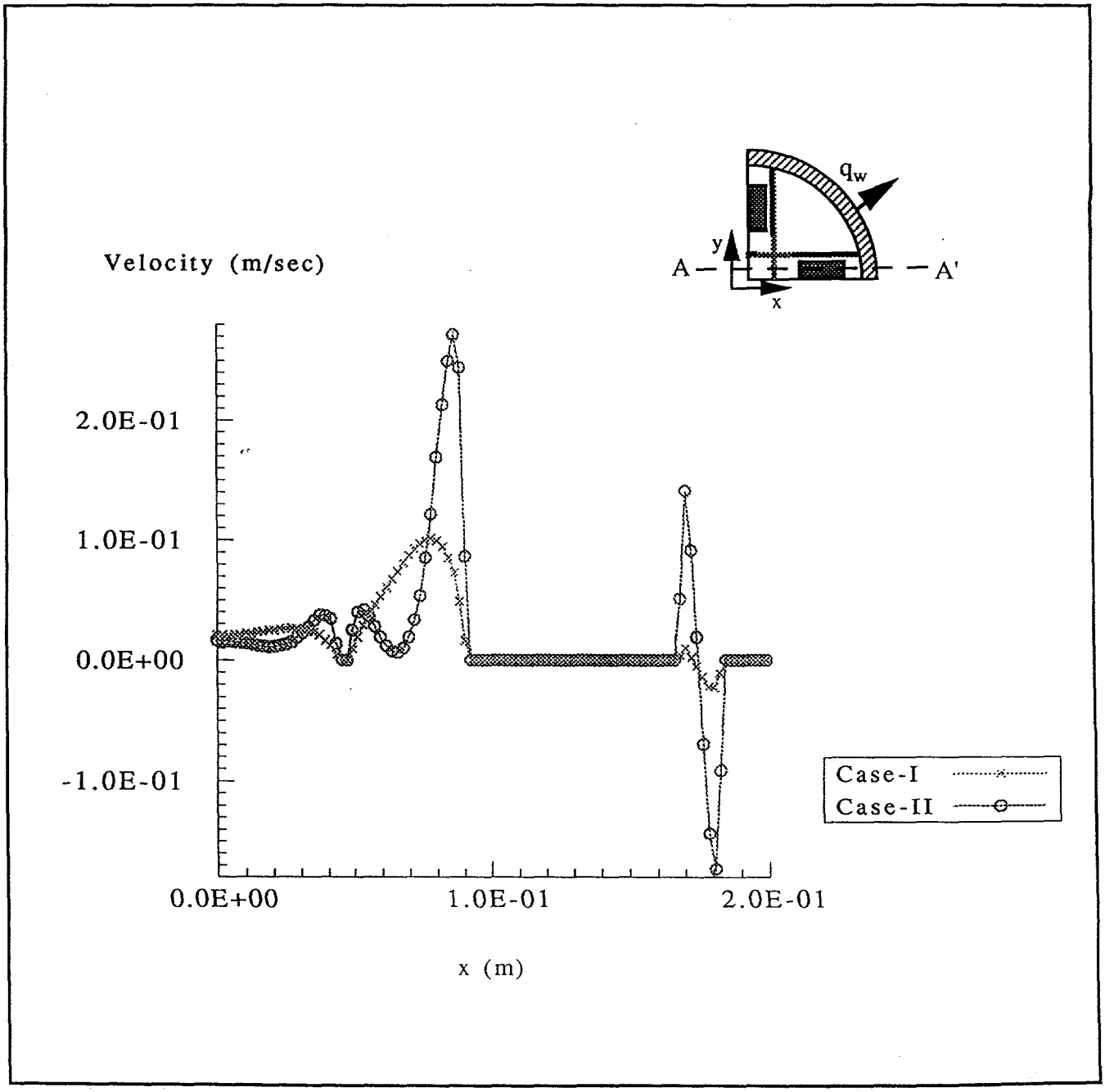

Figure 11. Velocity profiles for the conduction-convection model in Case-I and -II along the A-A' line (y=0.03175m) of the fuel mid-plane.

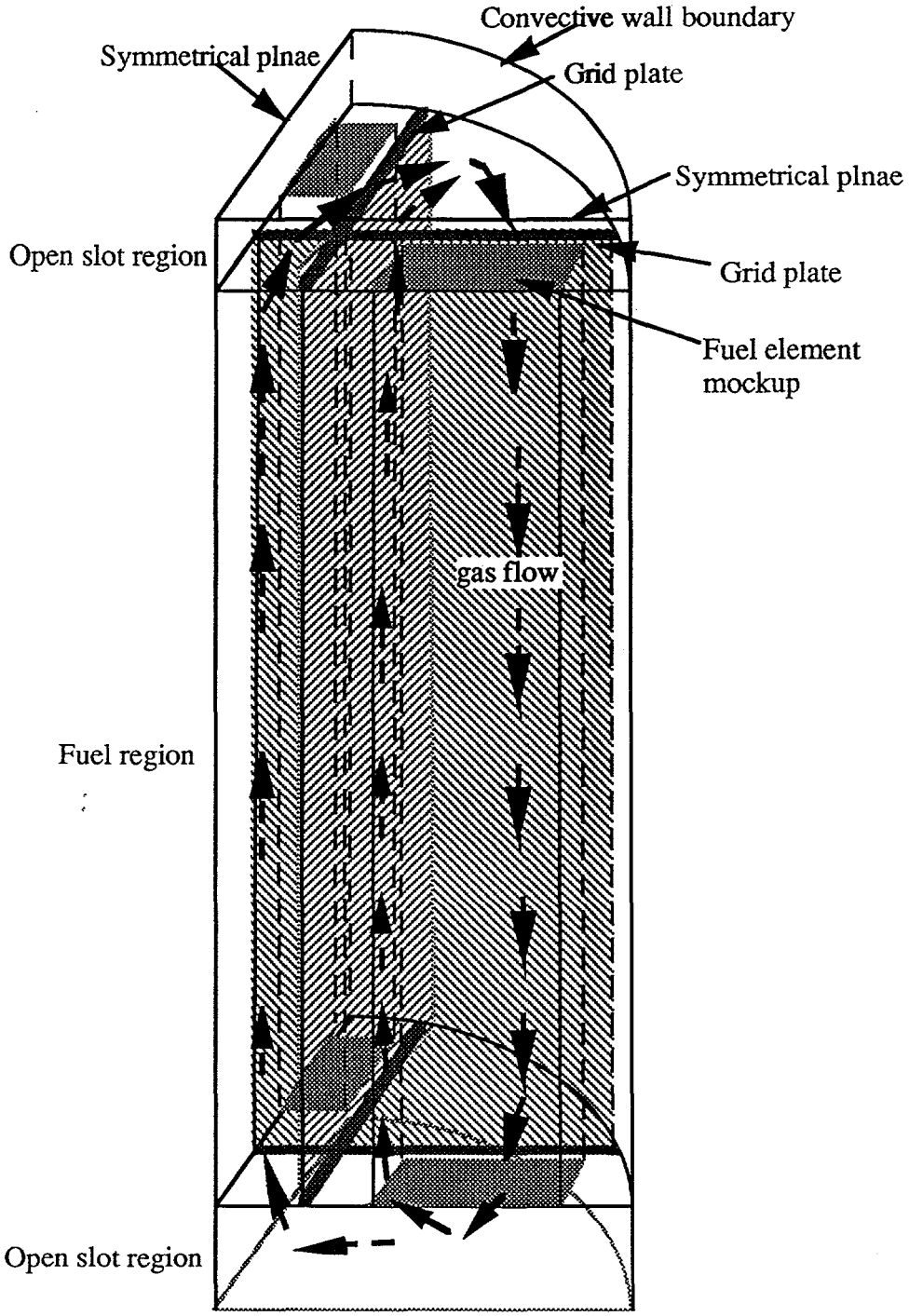

Figure 12. Gas flow pattern due to natural convection in the 90° sector model of an enclosed canister.

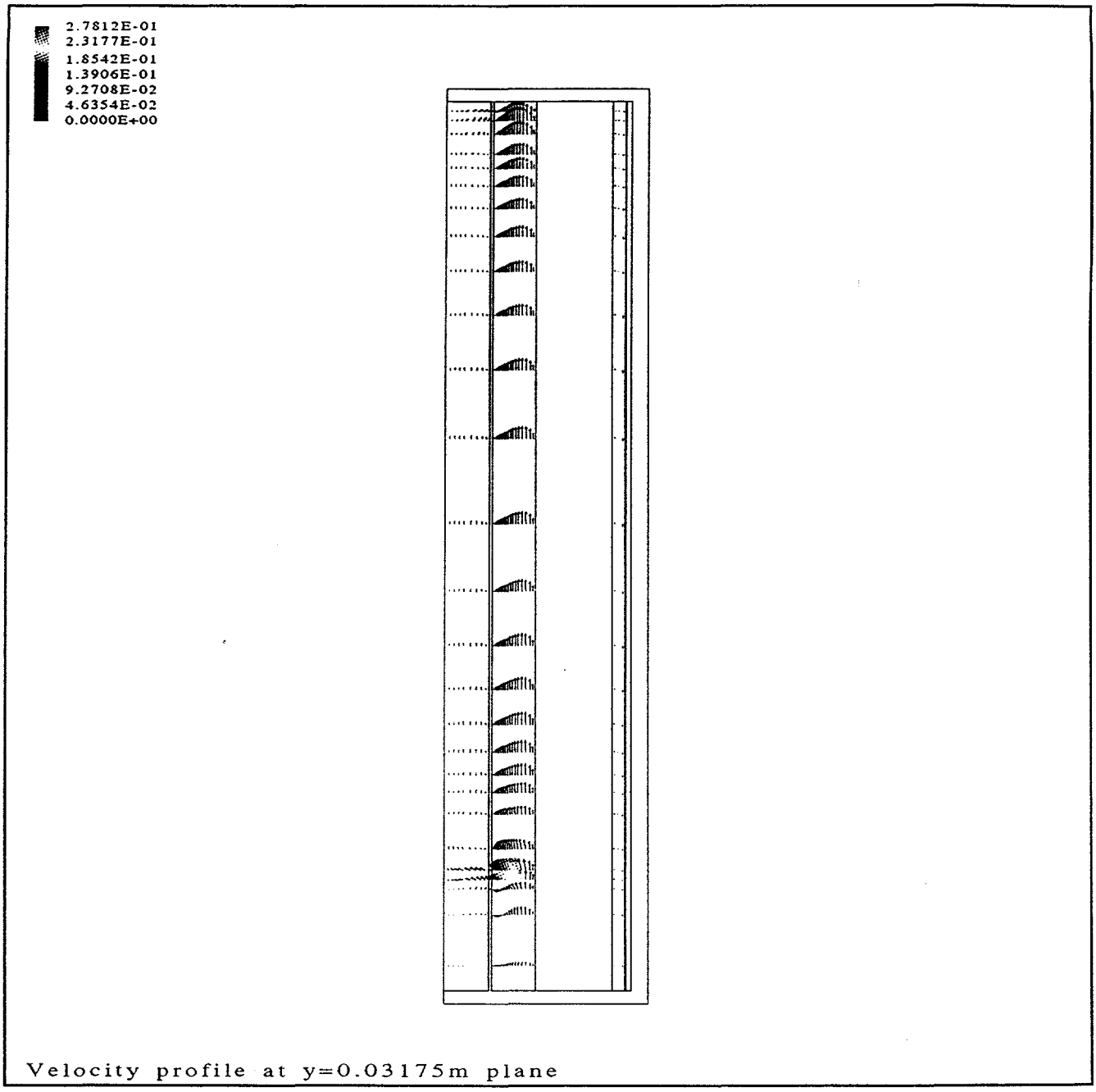

Figure 13. Velocity vector plot at y = 0.03175 m plane for Case-I.

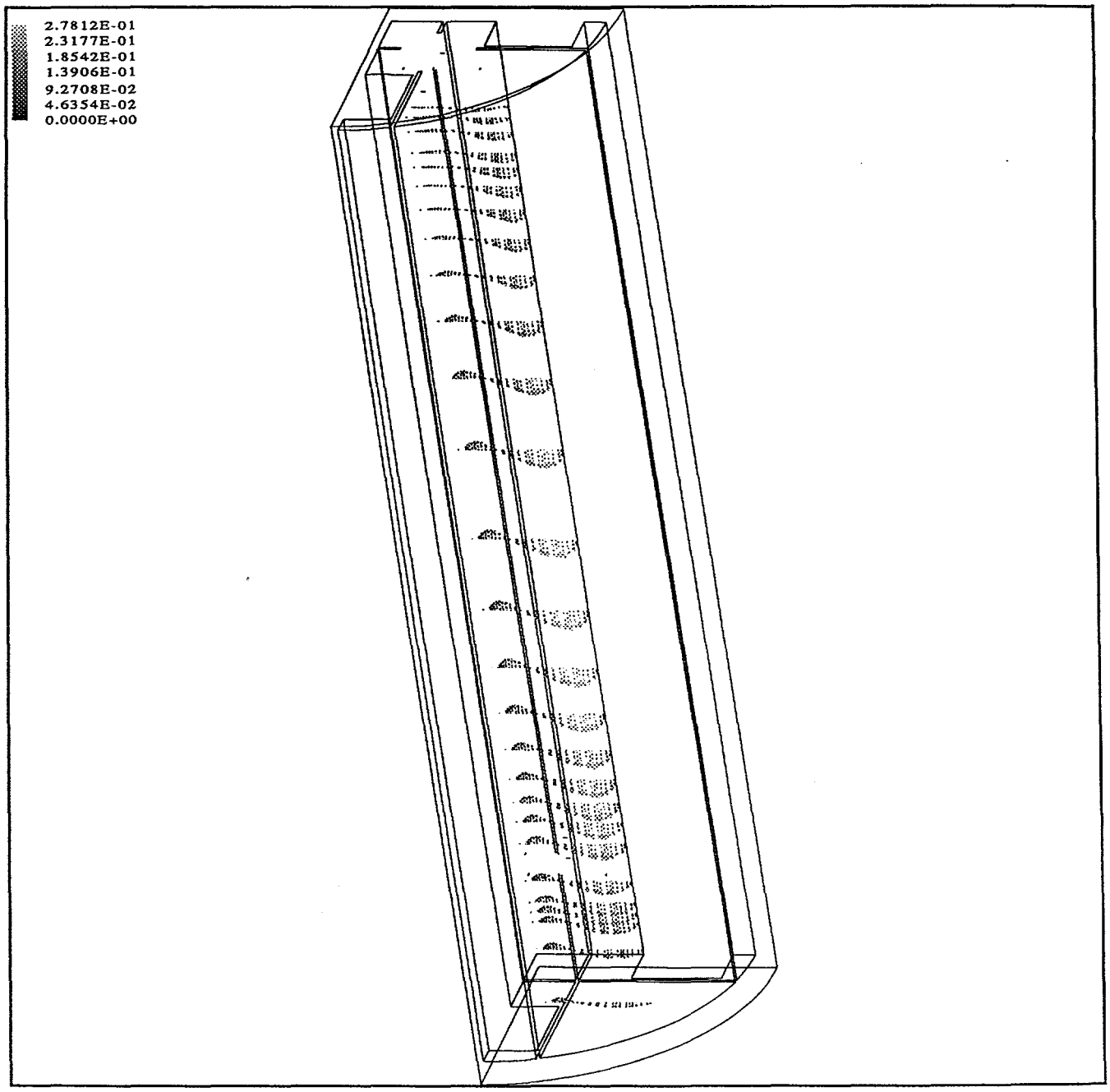

Figure 14. Velocity vector plot at y = 0.1294 m plane for Case-I.

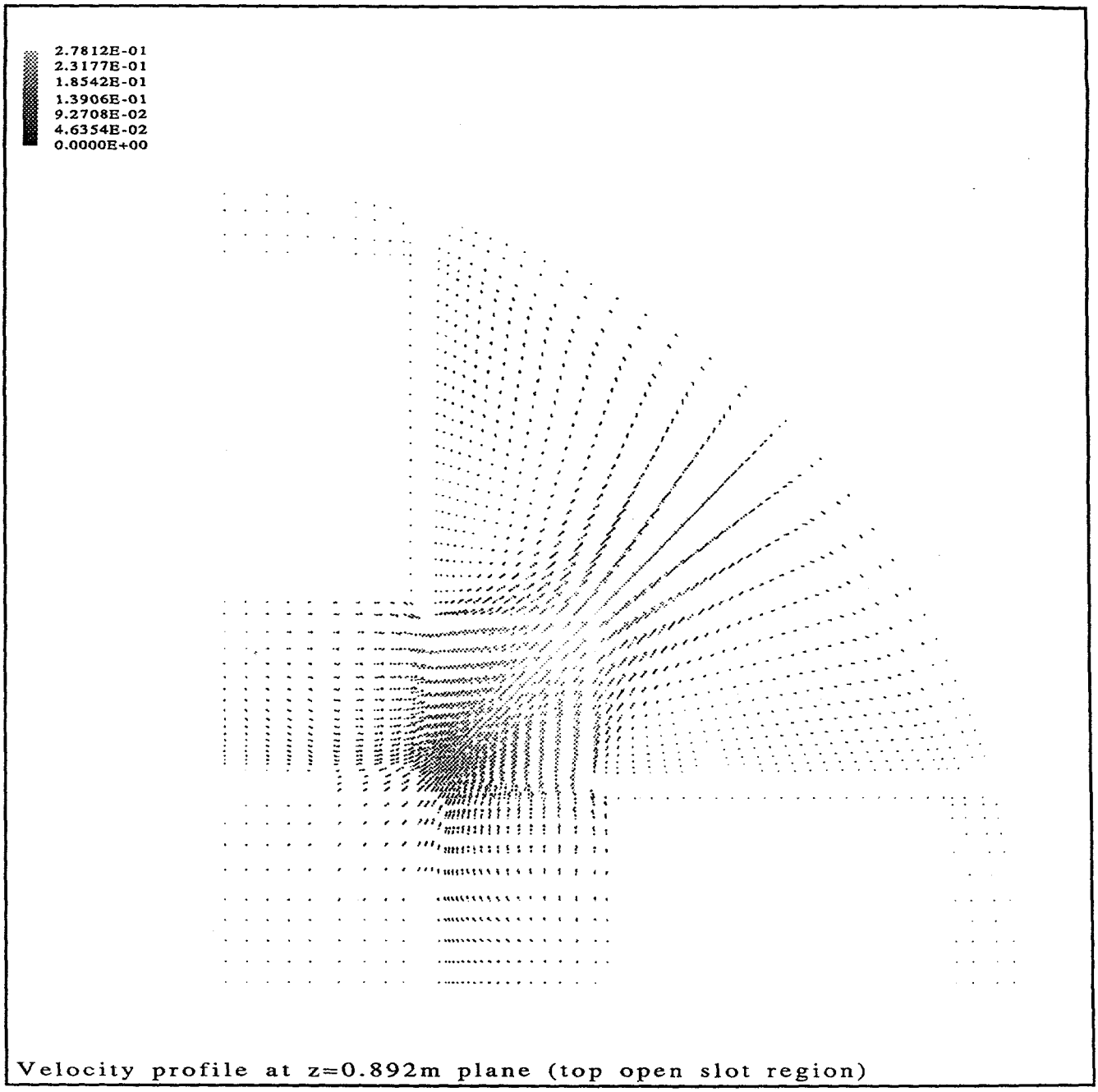

Figure 15. Velocity vector plot near top open slot region for Case-I.

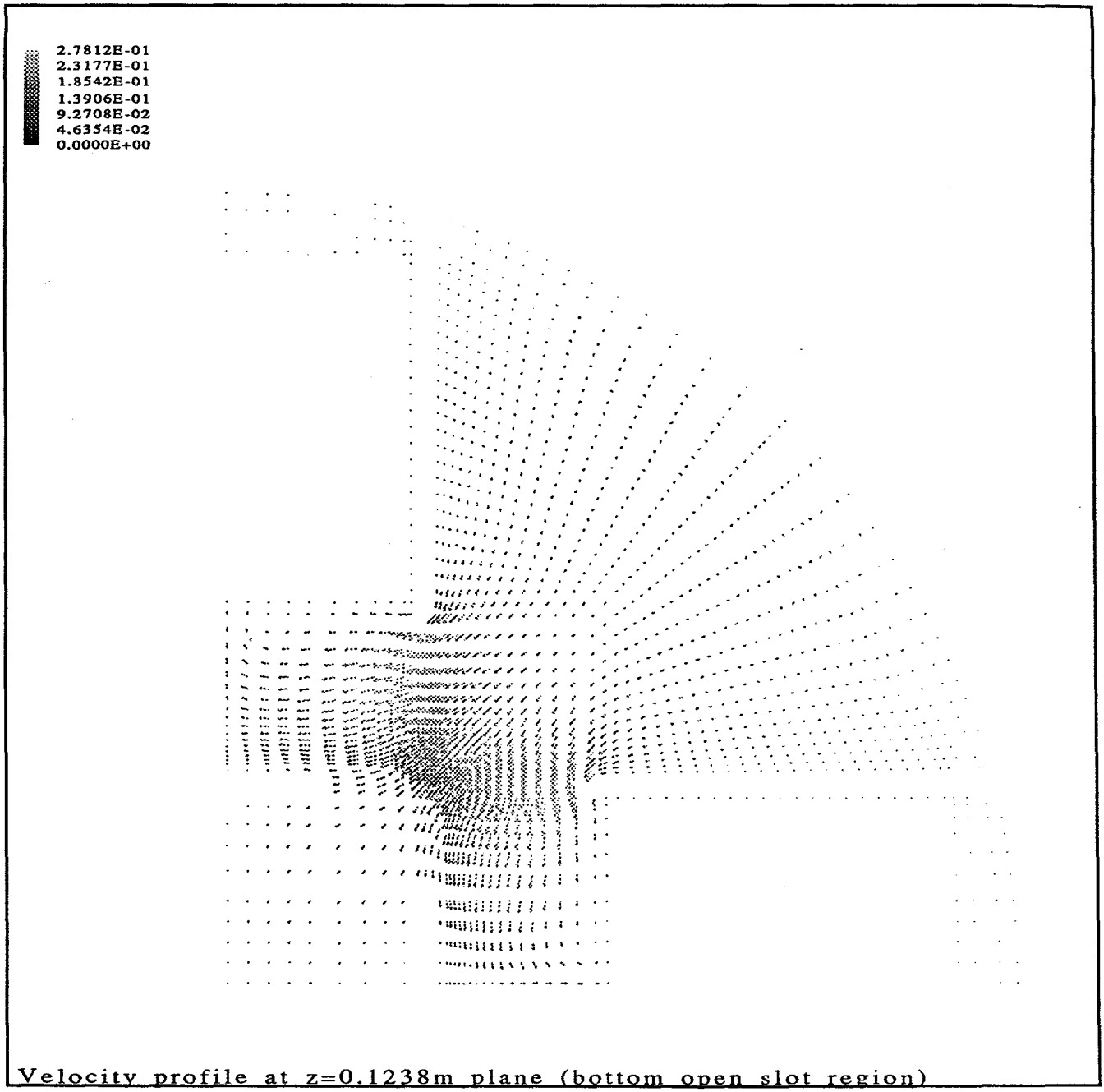

Figure 16. Velocity vector plot near bottom open slot region for Case-I.

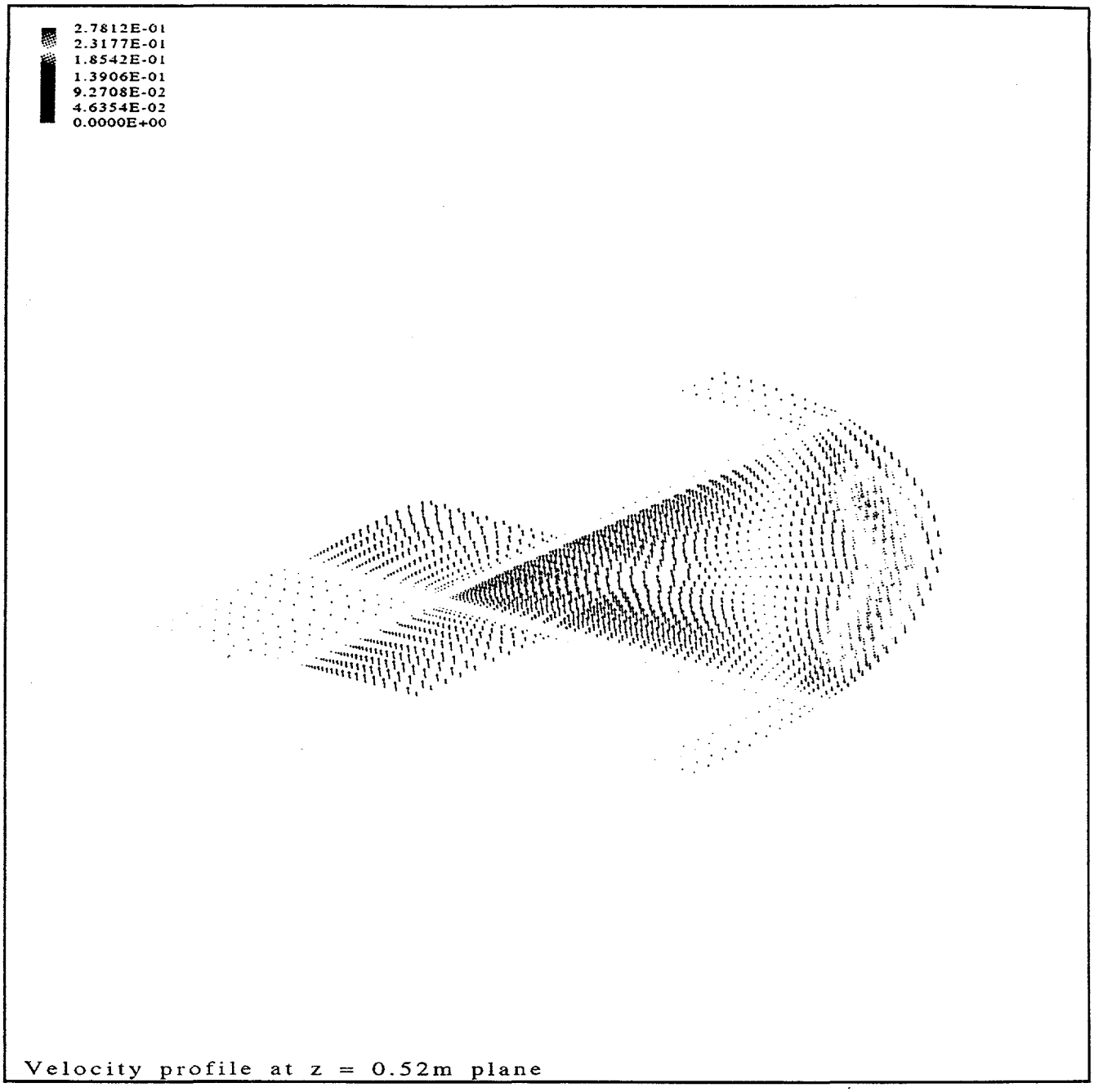

Figure 17. Velocity vector plot at the mid-plane of fuel region for Case-I.

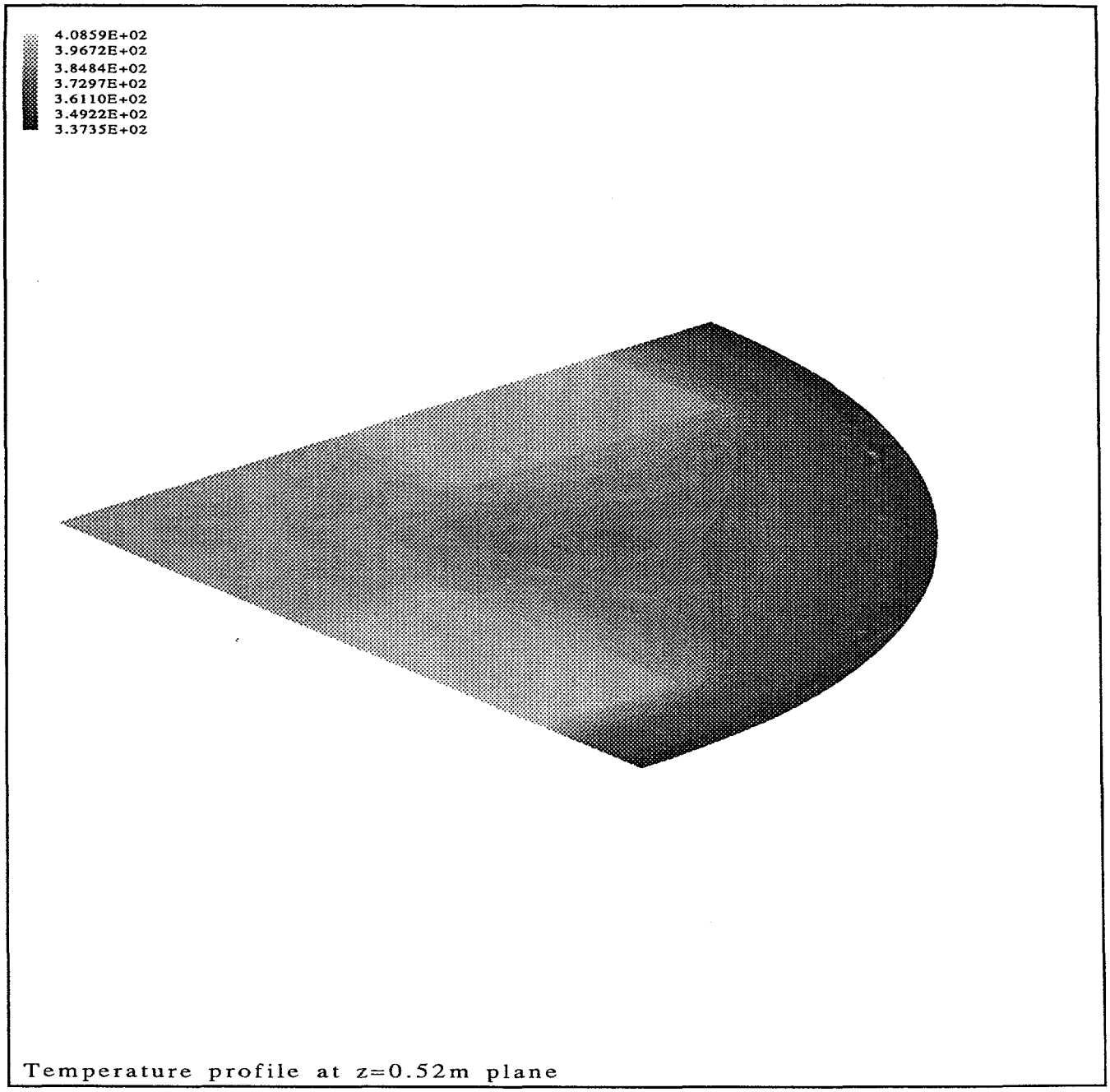

Figure 18. Temperature shaded contour plot at the mid-plane of fuel region for Case-I.

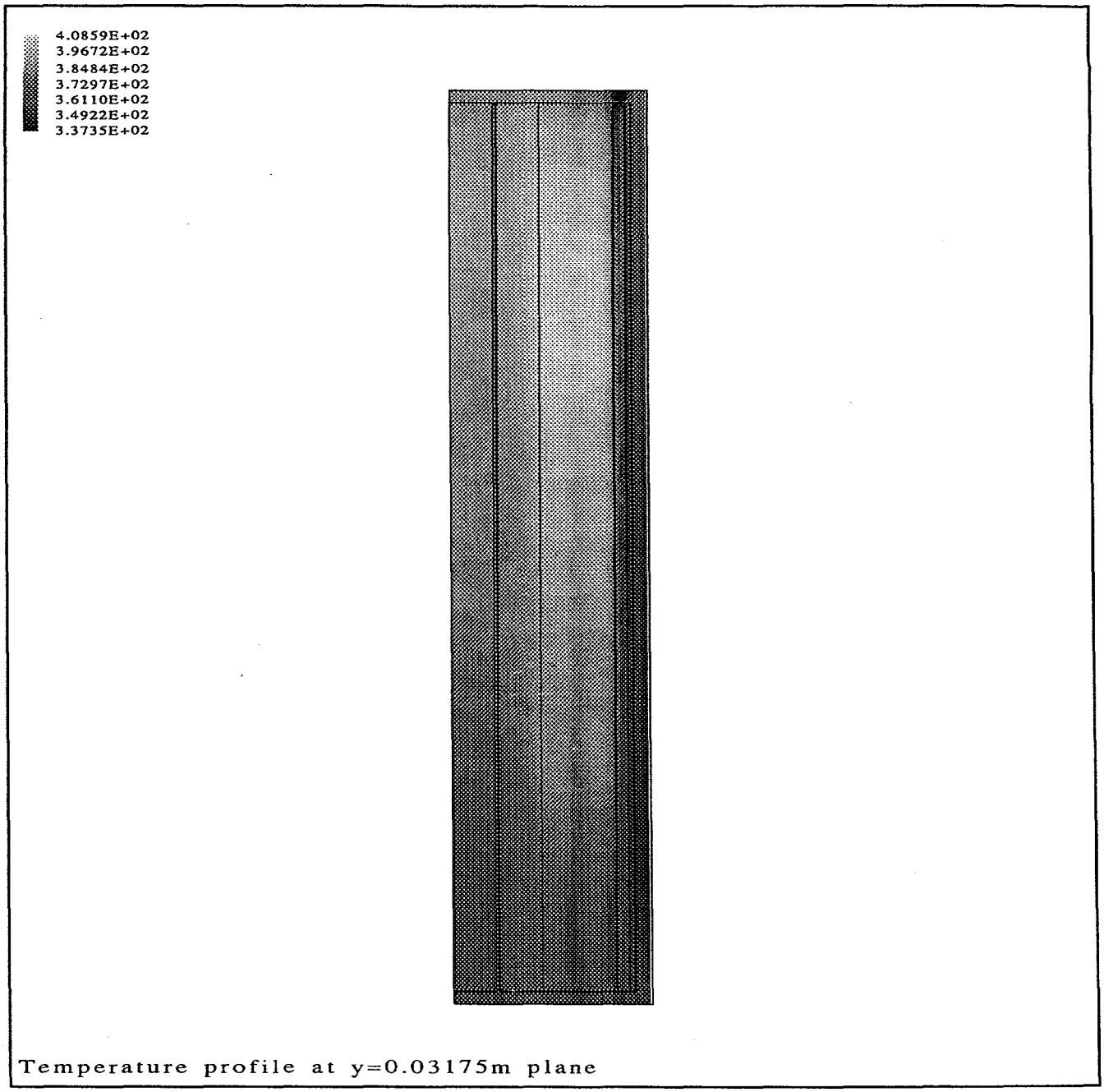

Figure 19. Temperature shaded contour plot at y=0.03175 m plane for Case-I.

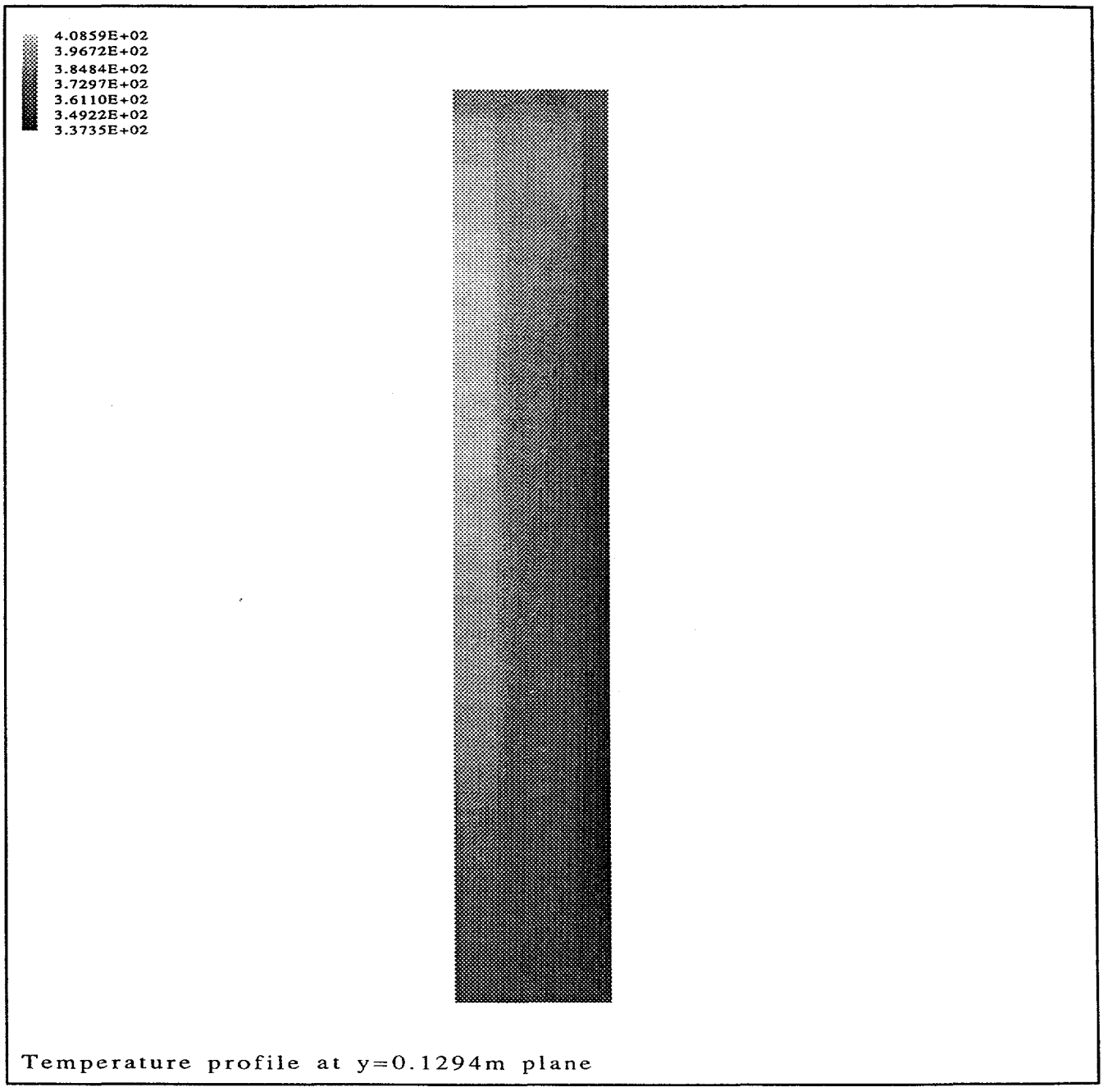

Figure 20. Temperature contour plot at y=0.1294 m plane for Case-I.

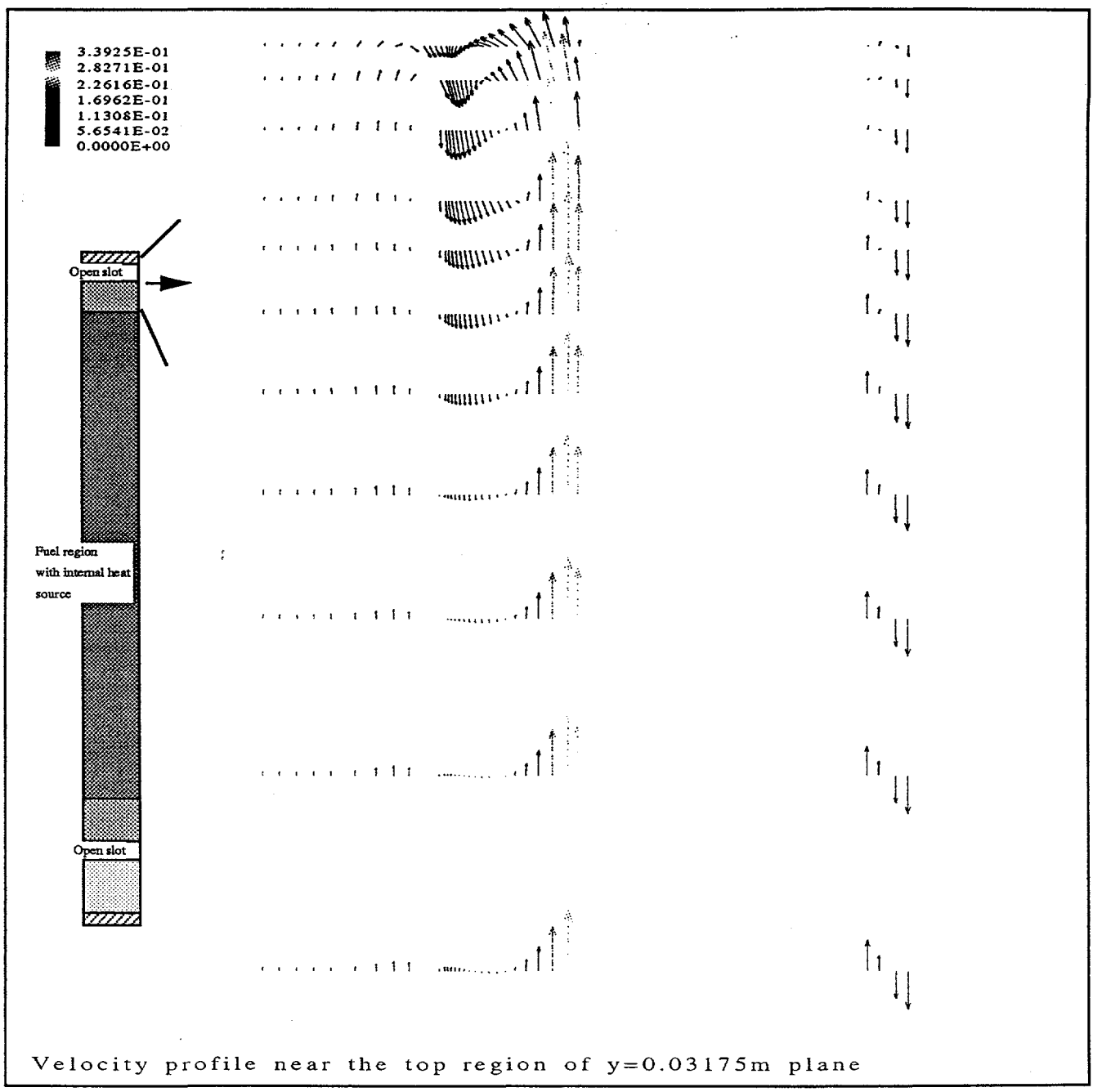

Figure 21. Velocity vector plot near the top region ($z \approx 0.889$ m) of y=0.03175 m plane for Case-II.

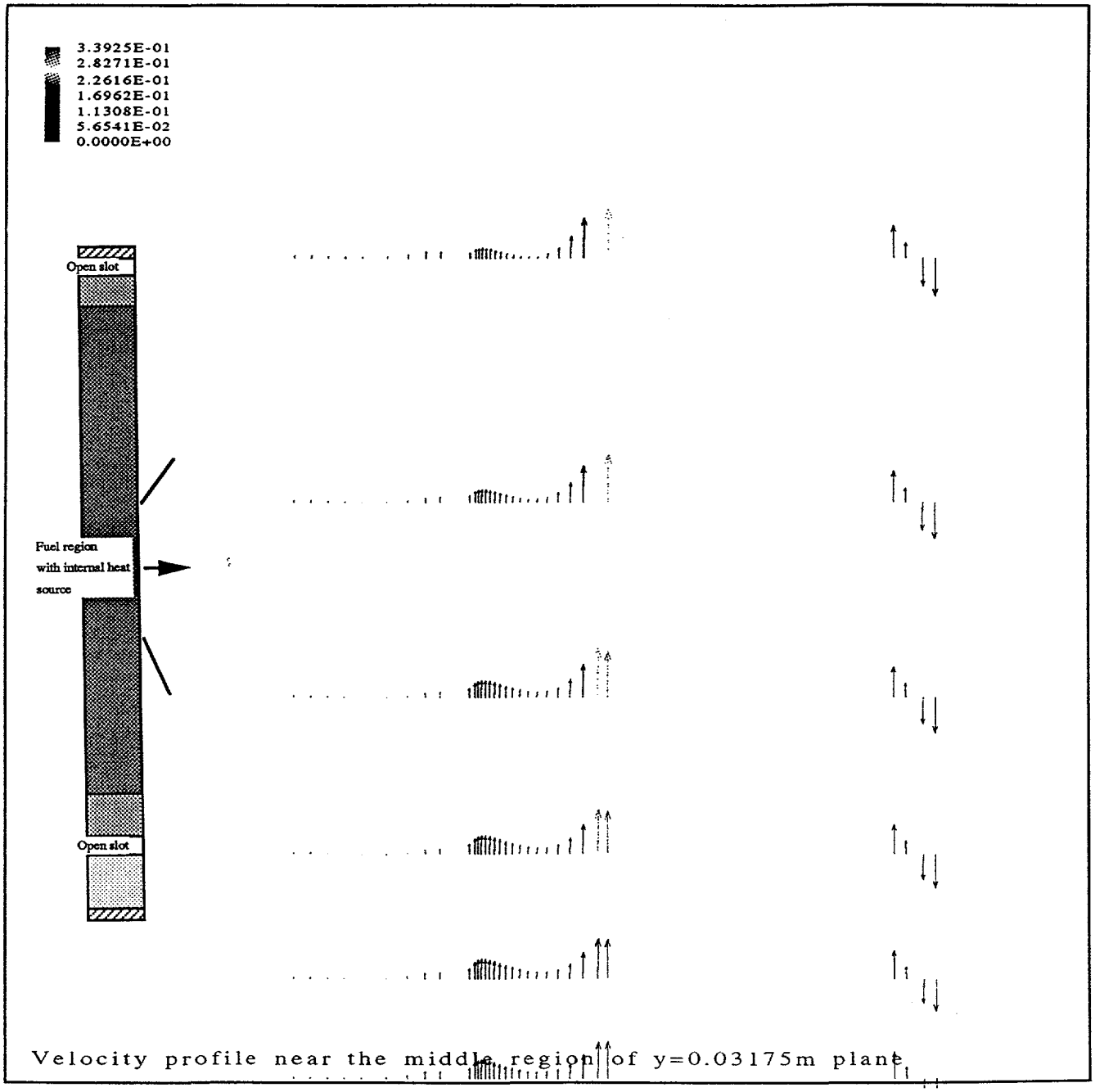

Figure 22. Velocity vector plot near the middle region ($z \approx 0.52$ m) of y=0.03175 m plane for Case-II.

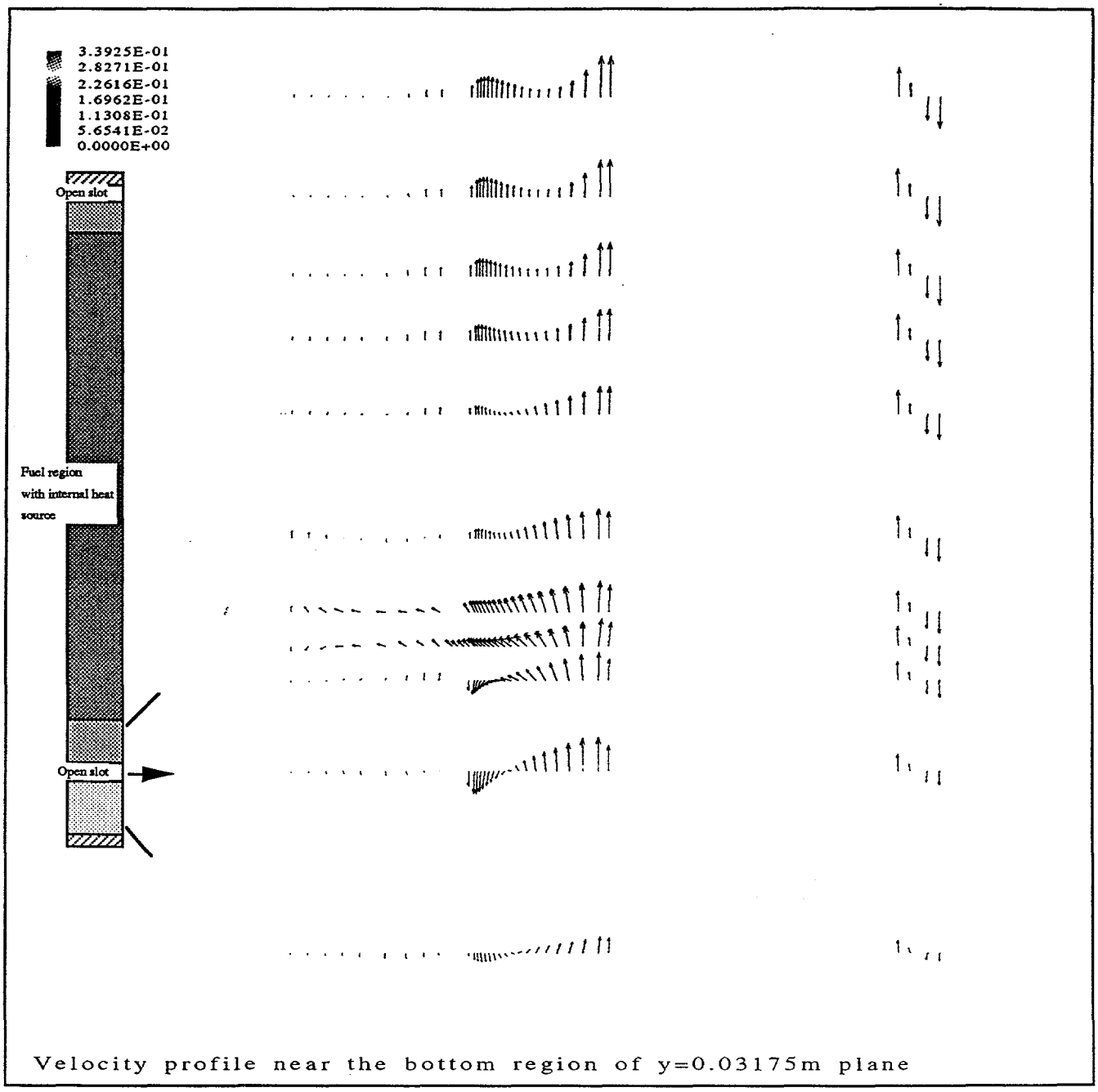

Figure 23. Velocity vector plot near the bottom region of y=0.03175 m plane for Case-II.

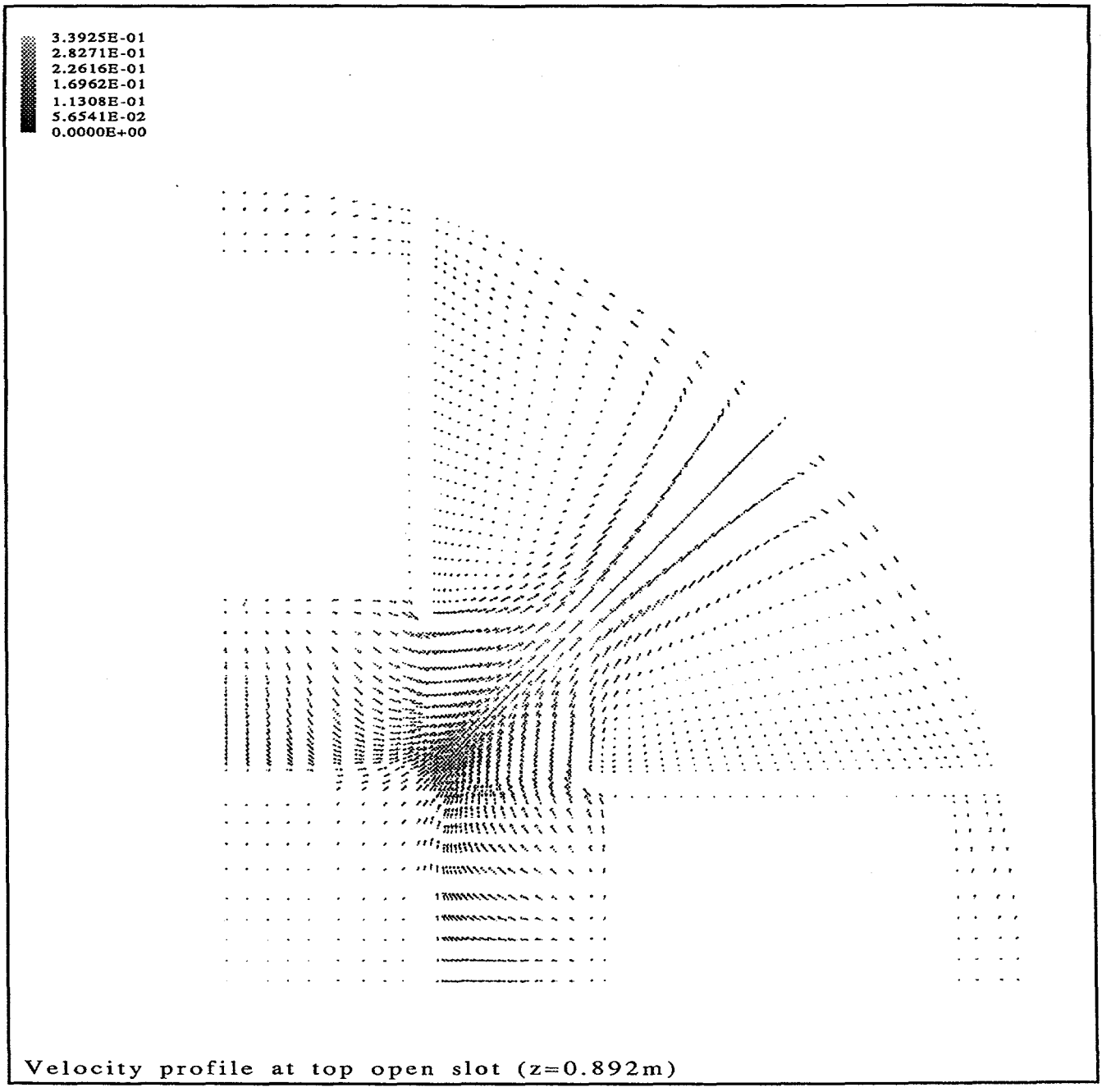

Figure 24. Velocity vector plot near the top open slot plane for Case-II.

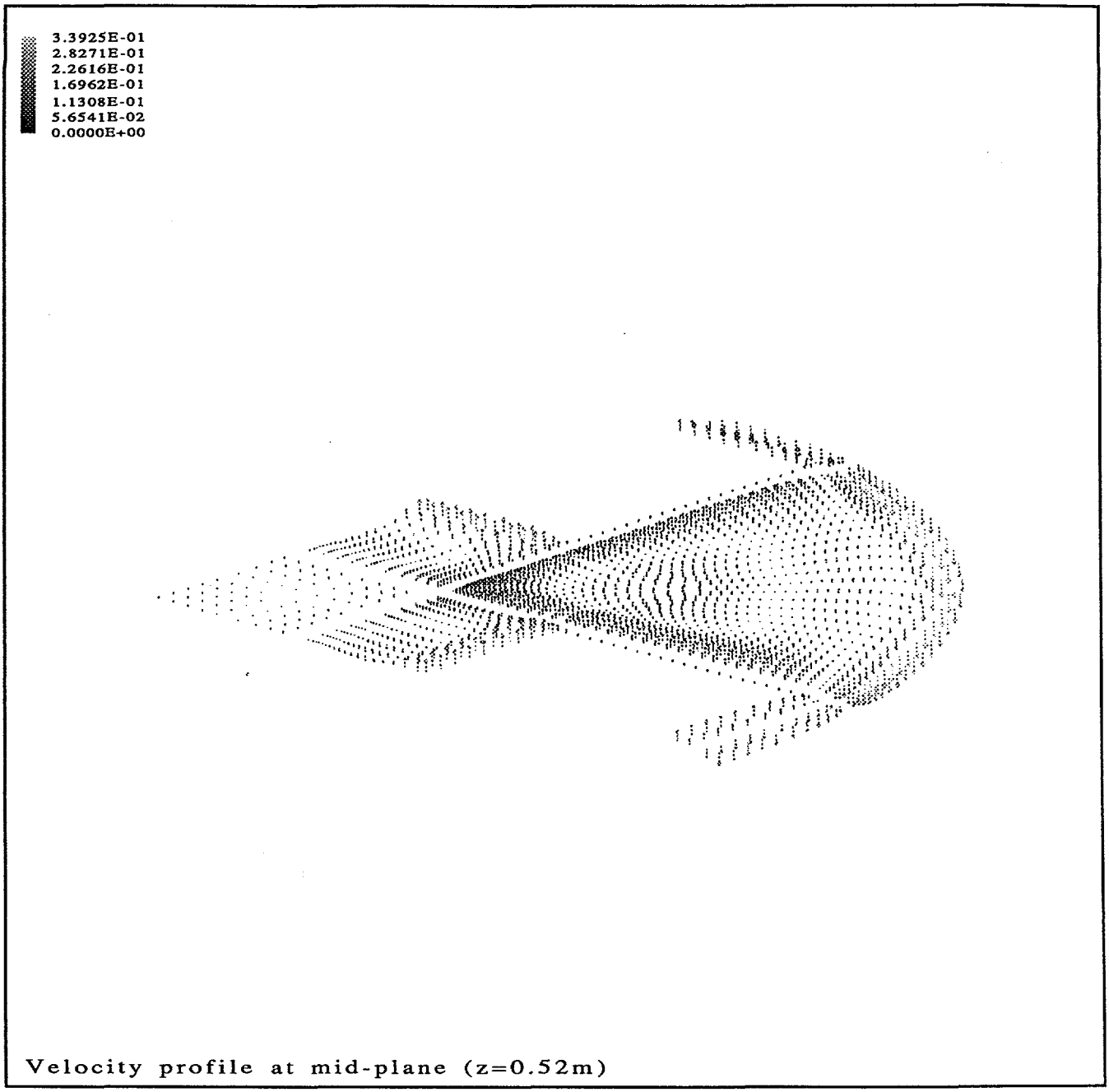

Figure 25. Velocity vector plot at the mid-height plane of the fuel region for Case-II.

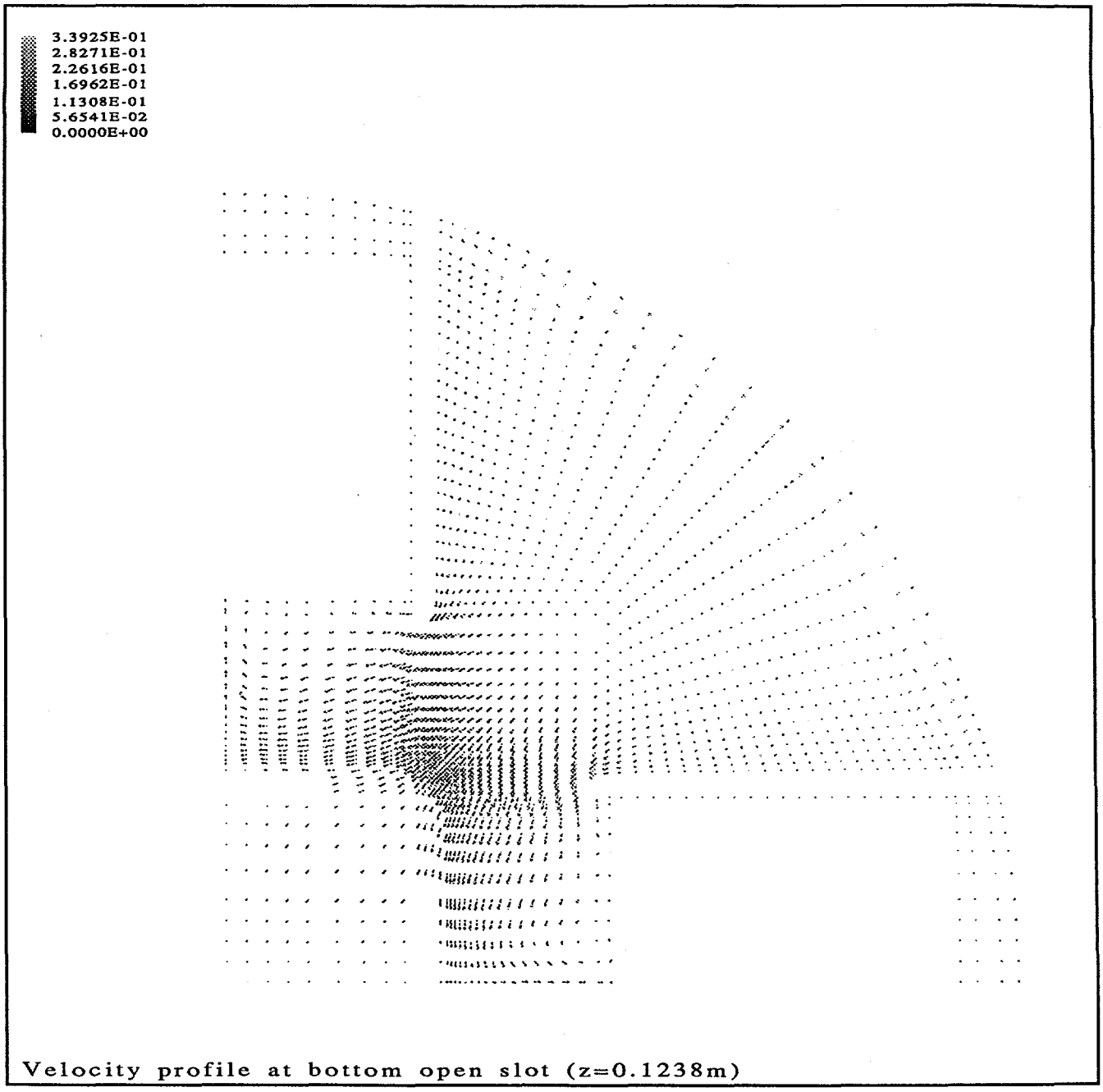

Figure 26. Velocity vector plot near the bottom slot plane for Case-II.

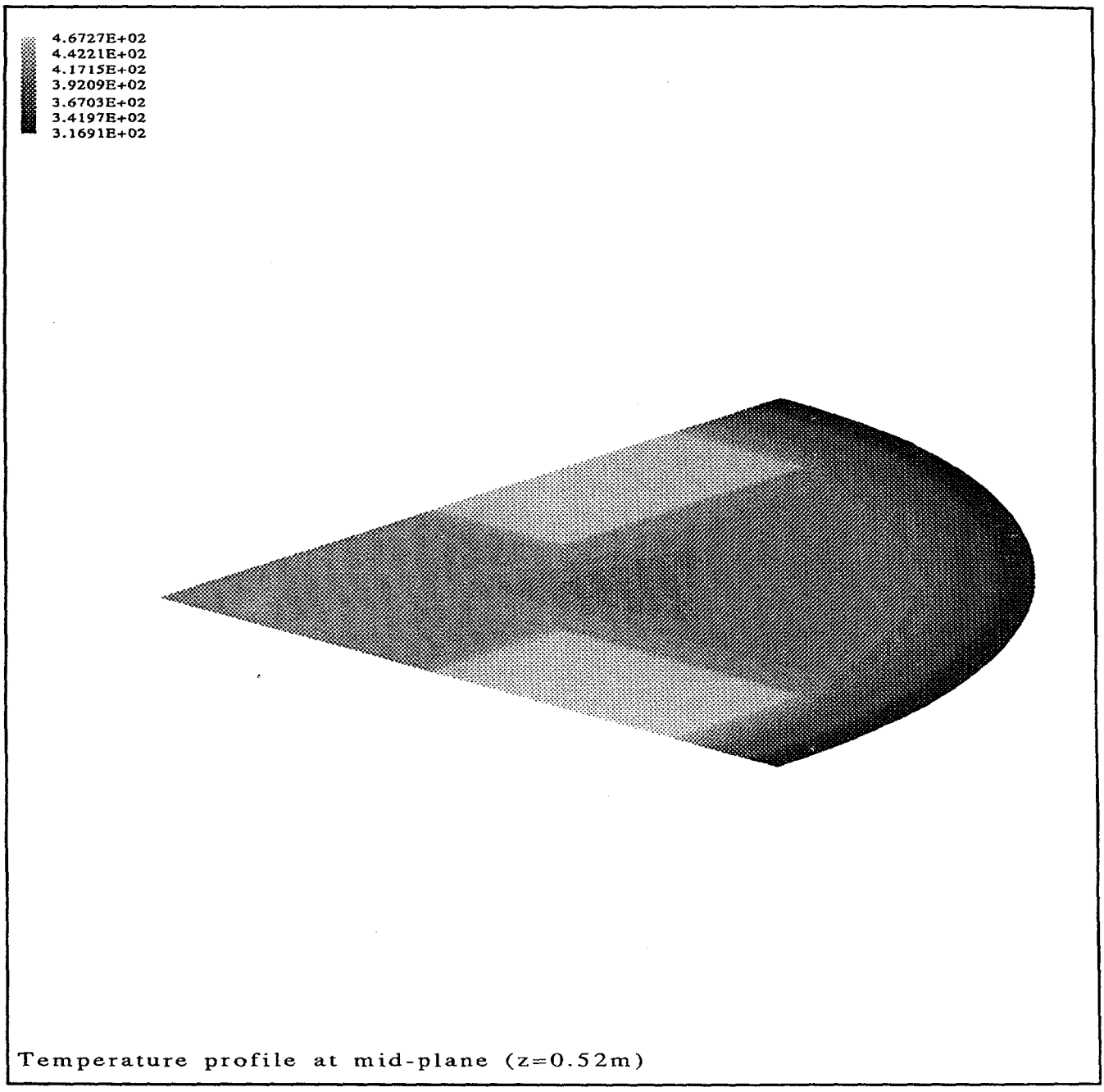

Figure 27. Temperature shaded contour plot at the mid-plane of fuel region for Case-II.

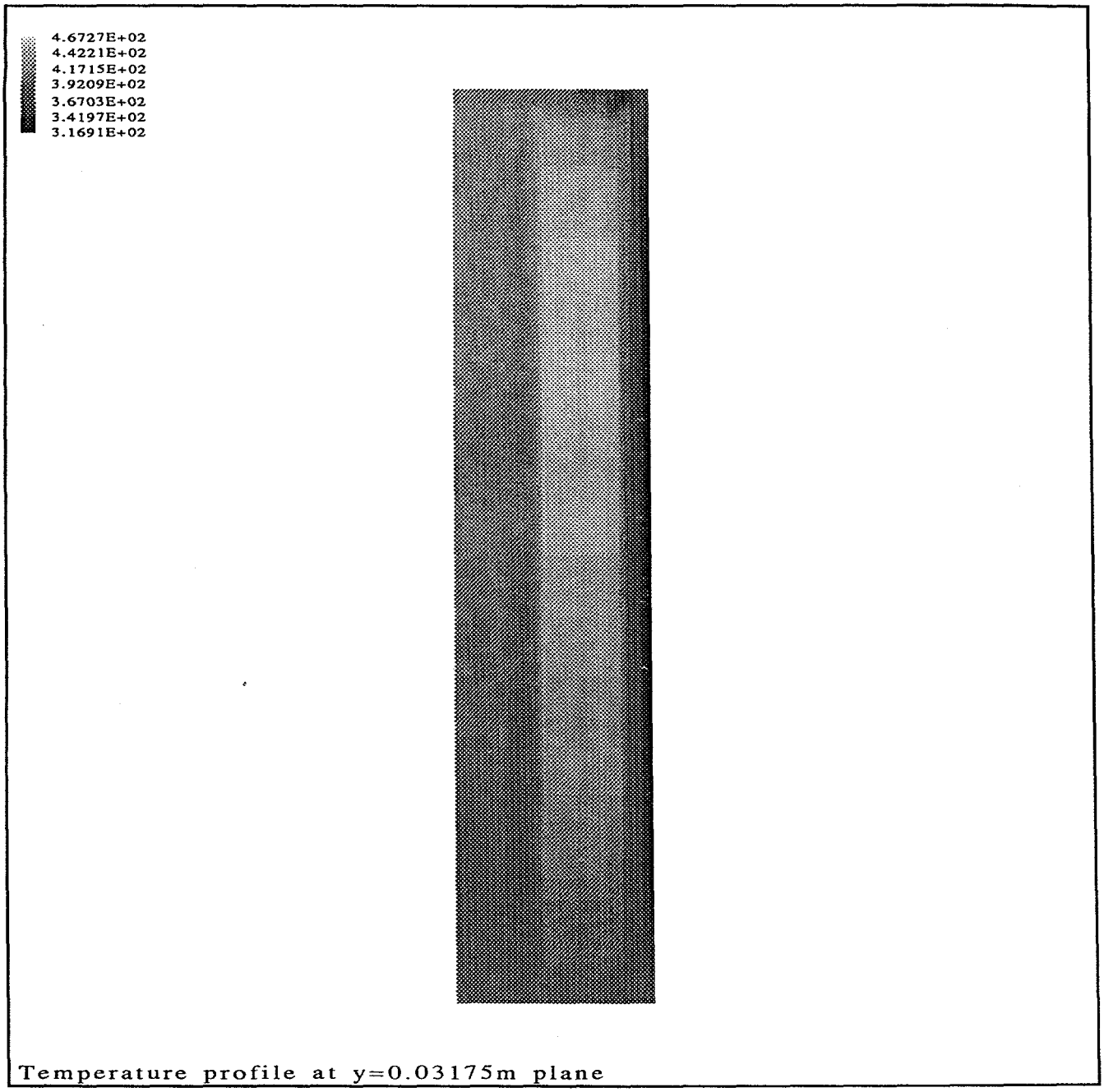

Figure 28. Temperature shaded contour plot at the y = 0.03175 m for Case-II.

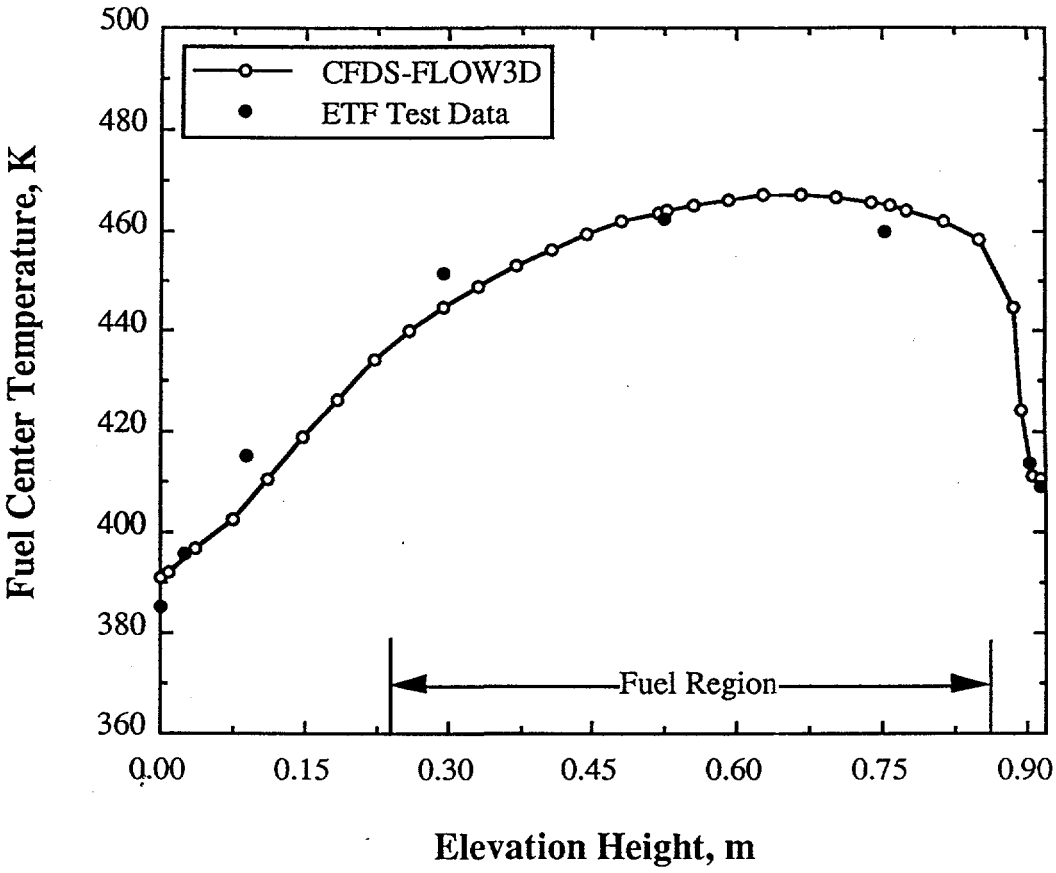

Figure 29. Temperature profiles for fuel center region along the vertical direction in Case-II.

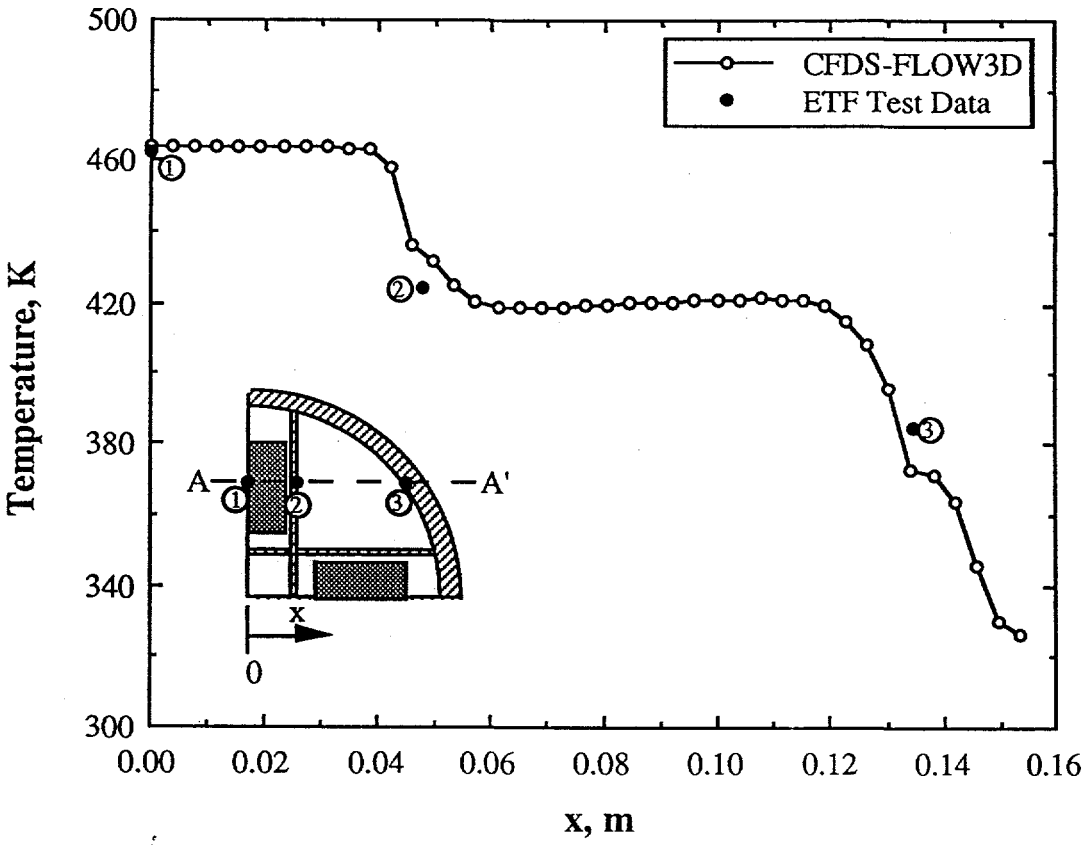

Figure 30. Temperature distributions along the A-A' line (y = 0.1294 m) of the fuel mid-plane in Case-II.

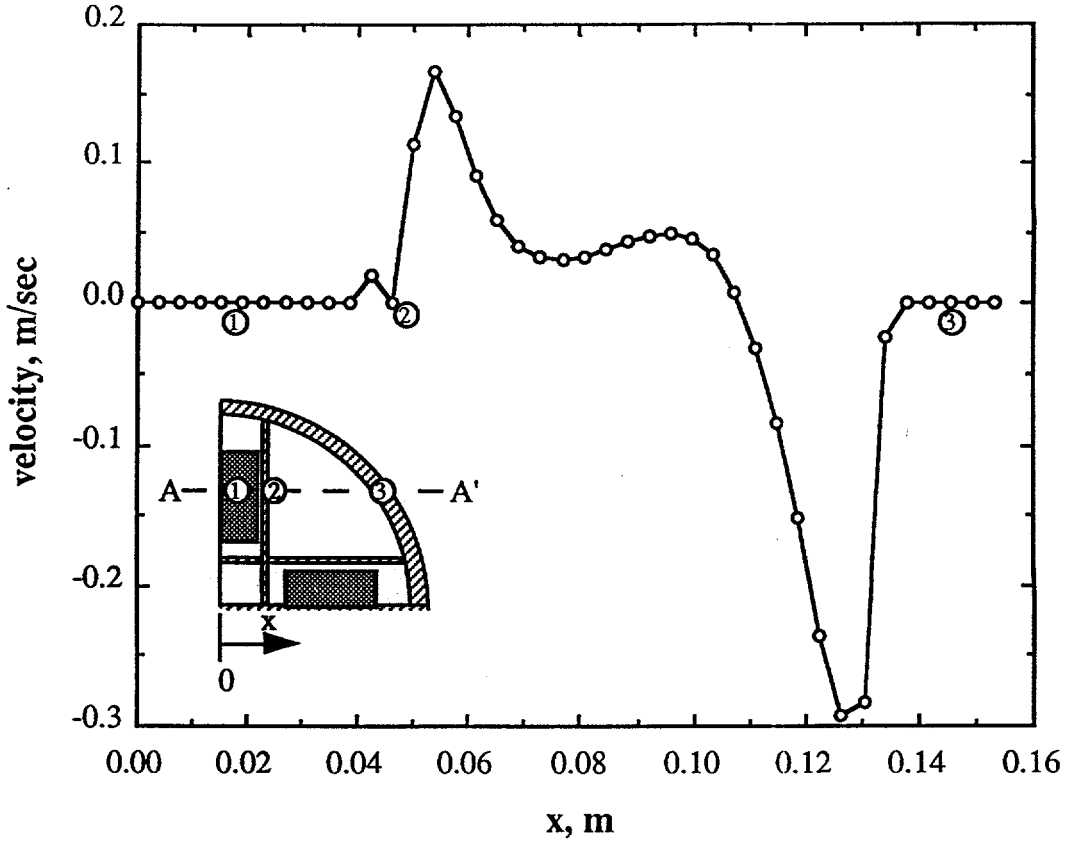

Figure 31. Velocity profile along the A-A' line (y = 0.1294 m) of the fuel mid-plane in Case-II.

References

1. Guerrero, H. N., "Interim Report - Spent Nuclear Fuel Technology Development Heat Transfer Study (U)", WSRC-TR-95-0202, May, 1995.

2. Eghbali, D. A. and Lee, S. Y., "Comparison of Conduction and Convection Heat Transfer Simulation Using the CFD Computer Codes FIDAP and FLOW3D (U)", SRT-ETF-950003, February 14, 1995.

3. McAdams, W. H., *Heat Transmission*, Third Edition, McGraw-Hill Book Company, 1954.

4. Eghbali, D. A, :Three-dimensional Thermal Analysis Simulation of Spent Nuclear Fuel Canister using FIDAP (U)", WSRC-TR-95-0184, April, 1995.

5. Kays, W. M. and Crawford, M. E., *Convective Heat and Mass Transfer*, Second Edition, McGraw-Hill Book Company, 1980.

6. Rohsenow, W. M. and Choi, H., *Heat, Mass, and Momentum Transfer*, Prentice-Hall, Inc. (1962).

7. Bird, R. B., Stewart, W. E., and Lightfoot, E. N., *Transport Phenomena*, John Wiley & Sons, 1960.